博士論文

Noninvasive monitoring of allograft rejection in a modified rat
lung transplant model: Application of machine learning-based
18F- fluorodeoxyglucose positron emission tomography
radiomics

(改良ラット肺移植モデルを用いた非侵襲的肺移植後拒絶反
応モニタリングの試み：18F- fluorodeoxyglucose positron
emission tomography の Radiomics 解析における機械学習の
利用)

田　東

TIAN Dong

博士論文

Noninvasive monitoring of allograft rejection in a modified rat lung transplant model: Application of machine learning-based 18F- fluorodeoxyglucose positron emission tomography radiomics

(改良ラット肺移植モデルを用いた非侵襲的肺移植後拒絶反応モニタリングの試み：18F- fluorodeoxyglucose positron emission tomography の Radiomics 解析における機械学習の利用)

Department of Thoracic Surgery

The University of Tokyo Graduate School of Medicine

Supervisor: Jun NAKAJIMA

Applicant: Dong TIAN

Table of Contents

Chapter 3: Noninvasive monitoring of allograft rejection in a rat lung transplant model: Application of machine learning-based 18F- fluorodeoxyglucose positron emission tomography radiomics

List of Abbreviations

6MWT	6-minute walk test
18F-FDG PET/CT	18F-fluorodeoxyglucose PET/CT
AR	Allograft rejection
AUC	Area under the curve
ANOVA	Analysis of variance
BOS	Bronchiolitis obliterans syndrome
CT	Computed tomography
CLAD	Chronic lung allograft dysfunction
CsA	Cyclosporine A
CI	Confidence interval
DC	Distance correlation
DCA	Decision curve analysis
GLCM	Gray level co-occurrence matrix
GLDM	Gray level dependence matrix
GLN	Gray Level Non-Uniformity
GLRLM	Gray level run length matrix
HE	Hematoxylin-eosin
ISHLT	International Society for Heart and Lung Transplantation
IFGN	Information gain
IMC	Informational Measure of Correlation
LASSO	Least absolute shrinkage and selection operator

LTx	Lung transplantation
LR	Logistic regression
LOOCV	Leave-one-out cross-validation
MCT	Methacholine challenge test
ML	Machine learning
MRI	Magnetic resonance imaging
MT	Masson's trichrome
NGTDM	Neighboring gray-tone difference matrix
NPV	Negative predictive value
PET	Positron emission tomography
PA	Pulmonary artery
PV	Pulmonary vein
PPV	Positive predictive value
ROI	Region of interest
RAS	Restrictive allograft syndrome
RFE	Recursive feature elimination
RF	Random forest
ROC	Receiver operating characteristic
RV	Run Variance
SUV	Standardized uptake value
SVM	Support vector machine
TBLB	Transbronchial lung biopsy

ABSTRACT

OBJECTIVE: To propose modifications of orthotopic rat lung transplantation (LTx) and construct machine learning (ML)-based positron emission tomography (PET) radiomics models for predicting AR in rat LTx.

METHODS: Initially, 180 consecutive rat LTx were performed using the modified technique. Twenty-eight recipient rats were served in PET experiment and set in four groups: isograft, allograft-cyclosporine$_{continuous}$ (CsA$_{cont}$), allograft-CsA$_{delayed}$, and allograft-CsA$_{1week}$. 18F-fluorodeoxyglucose PET was acquired at weeks 3 and 6 post-transplant, and the maximum standardized uptake value (SUV$_{max}$) and radiomics features were extracted from PET images. The least absolute shrinkage and selection operator algorithm was used to calculate a radiomics score (Rad-score). Eight modeling algorithms (seven ML algorithms and one logistic regression) with six feature selection methods were performed to develop 48 radiomics models for monitoring AR, validated using leave-one-out cross-validation.

RESULTS: I modified a rat LTx model with easy mastery, expeditiousness, no intraoperative complication or death. In total, 837 radiomics features were extracted from each PET image. The SUV$_{max}$ and Rad-score showed significant positive correlations with histopathology ($P < 0.05$). The median area under the curve (AUC) of 42 ML models was 0.944, superior to that of 6 logistic regression models (AUC, 0.794). The optimal ML model using a random forest modeling algorithm with random forest feature selection method exhibited the highest AUC of 0.978 in all models.

CONCLUSION: I modified the rat LTx model and demonstrated SUV$_{max}$ provided a

good correlation with AR, but ML-based PET radiomics further strengthened the power

of 18F-fluorodeoxyglucose PET functional imaging for monitoring AR in LTx.

Chapter 1: General introduction

1.1 Challenges

Lung transplantation (LTx) is the only therapeutic option for end-stage lung diseases. Although substantial progress in LTx, both experimental and clinical settings, has been made in the past decades, postoperative recipient survival remains short of the anticipated goal compared with other solid organ transplantations [1, 2]. LTx recipients have a median survival time of 6.7 years, and the 5-and 10-year unadjusted survival rates are 54% and 32%, respectively [3, 4].

Lung allograft rejection (AR), including acute rejection and chronic rejection, predominantly results in chronic lung allograft dysfunction (CLAD), is a major post-transplant complication. Acute rejection, mainly including acute cellular rejection and antibody-mediated rejection, occurs anytime with an incidence of 27.3% in the first year after transplant and is responsible for approximately 4 % of deaths in the first 30 days following transplantation [1]. It is a change that develops silently without obvious symptoms which may recover with prompt treatment. In some cases, nonspecific symptoms like shortness of breath, cough, or a low-grade fever may be presented. Over time, it may deteriorate into CLAD, manifesting as airflow restriction and/or obstruction. Half of all lung recipients will develop CLAD in 5 years, and this rate may increase up to 75% ten years after surgery owing to the paucity in accurate and effective early detection and treatment methods [5, 6]. CLAD, limiting the survival of patients after surgery, comprises two phenotypes mainly based on pulmonary function and radiographic findings: bronchiolitis obliterans syndrome (BOS) and restrictive allograft syndrome

(RAS) [7]. BOS is the predominant phenotype, accounting for 75-85% of CLAD cases. Median allograft survival is approximately four years after BOS onset [8]. In contrast, RAS is commonly presented as a more aggressive functional deterioration and has a worse prognosis, with median allograft survival of < 2 years and first proposed by Sato and colleagues in 2011 with approximately 25-35% of all CLAD cases [7-9]. AR and transplant failure place a huge burden on both patients and healthcare systems, and early detection of lung AR is of great significance for the prognosis of LTx. Therefore, accurate early detection and prophylactic strategies against AR are urgently required to slow or stop disease progression [4].

1.2 Transbronchial lung biopsy (TBLB)

TBLB is considered the gold standard for AR diagnosis, especially in acute rejection, and is frequently performed for routine monitoring during the first year after transplantation, but is limited by the likelihood of pneumothorax, bleeding, sampling error, and inter-observer variability of biopsy interpretation [10-12]. Additionally, the airways in living-donor lobar LTx patients are relatively smaller, which may cause difficulties in performing bronchoscopy. Therefore, TBLB may not be performed during the entire lifespan of the graft since its risks may outweigh the possible benefits [4]. For such a high-risk detective strategy, noninvasive examinations with considerable sensitivity and specificity are favored by clinicians.

1.3 Clinical symptoms and spirometry

Clinical symptoms are the straightforward way to diagnose AR. However, the early symptoms and signs of rejection are nonspecific, and the onset of rejection and decline in pulmonary function often occur before the onset of clinical symptoms [13, 14]. Spirometry has been found to have a sensitivity of greater than 60% for detecting acute rejection grade A2 and higher [15]. The CLAD, including BOS, RAS, mixed, and undefined, is primarily characterized by spirometry [7, 16]. Spirometry should be performed continuously over a long period and is characterized by lower associated costs. However, some allograft or extra-allograft factors can result in a persistent decline in pulmonary function. Single LTx recipients assessed only by pulmonary function tests (PFT) may be misdiagnosed because of the confounding effects of the native lung [17]. In addition, the evaluation of pulmonary function in pediatric LTx patients is difficult, especially in children aged below four years [8].

1.4 Imaging examinations

1.4.1 Conventional imaging examinations

Conventional imaging examinations, including chest X-ray, Computed tomography (CT), Magnetic resonance imaging (MRI), lung ultrasound, and others, have been reported as the noninvasive methods for detecting AR, but the controversy remains. Chest X-ray is relatively insensitive and non-specific to the diagnosis of acute rejection. It is difficult to distinguish acute rejection from reimplantation response and pneumonia in the early postoperative period by the radiographic appearance [18]. Findings on chest X-ray are

usually normal in the early stages of CLAD, which is slightly unlike those in the early stages of acute rejection [19, 20]. Despite this, some nonspecific abnormal warning signals for AR may be observed in chest radiographs. CT is considered the core examination that is performed during continuous follow-up. However, previous studies have revealed that CT imaging has limited accuracy for assessing acute rejection [21, 22]. Compared with indirect measurements such as clinical symptoms and spirometry, CT examination may allow the direct detection of CLAD [23]. Although there is limited information regarding the predictive value of CT in diagnosing CLAD development before symptoms occur, CT has many advantages in identifying disease progression at disease onset. MRI is a powerful imaging technology widely used to assess both pulmonary function and anatomical structure. Recent studies have revealed the great potential of the above methodologies for the early diagnosis of AR; however, confirming their value requires more institutional and large-sample prospective studies[24-26]. Lung ultrasound has been used in LTx, both clinical and basic studies, but it cannot reveal early AR [27-31].

1.4.2 Positron emission tomography (PET)

18F-fluorodeoxyglucose (FDG) PET/CT can provide both functional information and tissue details and is gradually applied to solid organ transplant examination [32-35]. In other organ transplantations, 18F-FDG PET/CT was used for diagnosing acute or chronic rejection and could monitor the efficacy of perioperative therapy [32, 33, 36, 37]. In the field of lung disease, 18F-FDG PET/CT has increasingly been utilized to predict

prognosis in idiopathic pulmonary fibrosis, malignancy, infection, and diffuse parenchymal lung disease [38-41]. Additionally, an animal study demonstrated that 18F-FDG PET imaging could lead to the rapid differential diagnosis of infection and inflammation due to the local availability of equipment and labeled agents [42]. In terms of LTx rejection, PET can provide more intuitive judgments on the anatomical markers of native and transplanted lungs during episodes of respiratory disease compared to PFTs during episodes of respiratory disease [43]. Daly et al. [33] assessed small animal PET imaging in a murine cardiac rejection model. It was found that PET imaging with FDG could be used as a noninvasive, quantitative technique for serial monitoring of allograft rejection. Chen et al. [44] demonstrated increased 18F-FDG uptake in allografts with acute rejection in a mouse model. However, clinical data from Jones et al. indicated that a high 18F-FDG PET signal was indicative of infection but not rejection in lung transplant recipients [45].

Although 18F-FDG PET is a controversial method for detecting acute rejection in LTx patients, studies on CLAD have shown positive results. A previous case report demonstrated hypermetabolic activity by18F-FDG PET imaging in RAS patients treated after pirfenidone treatment, which could indicate active fibroproliferation and pleuroparenchymal changes [46]. Recently, Verleden et al. [35] conducted a retrospective study of patients subjected to18F-FDG PET/CT scan and reported increased pulmonary 18F-FDG uptake in patients with RAS compared with patients with BOS. Moreover, 18F-FDG PET/CT can distinguish between the two phenotypes with a sensitivity of 76% and a specificity of 87%. Although 18F-FDG PET/CT scan may hold great potential for

detecting CLAD, certain drawbacks need to be resolved. The high cost may limit its routine use during follow-up. Additionally, the predictive value rather than just the diagnostic value of PET/CT should be confirmed in the future.

1.5 Hypothesis of the project

Noninvasive examination for the detection of AR remains a challenge: advantages and disadvantages always co-manifest. To date, no method has been demonstrated to verify AR with unequivocally ideal specificity and accuracy. Evidence has recently shown that radiomics was the noninvasive advanced imaging analytics with high accuracy in disease diagnosis and treatment evaluation [47, 48]. Radiomics can quantify the spatial correlations among image voxels that aims to relate the amount of imaging information to clinical outcomes. The application of radiomics analysis to graft rejection was only recently reported, with a study proposing that texture analysis applied to ultrashort echo time MRI might be a valuable tool for distinguishing AR in a mouse LTx model [49]. However, many features correlated with AR were not extracted from the images. Furthermore, the authors did not merge the radiomic features but only analyzed them separately [49]. Thus, their strategy could not reveal the inherent detective ability of radiomics for AR.

Because of its high-dimensional nature (which seems to be ever-growing as research continues), the field of radiomics needs powerful analytical tools. Machine learning (ML), a branch of artificial intelligence, appears to be a potential candidate for this purpose, having shown powerful capabilities in radiological research [50]. Currently, studies

reporting the use of ML algorithms to detect lung AR are low in number [51, 52]. Barbosa et al. [51] reported that an ML algorithm using quantitative CT metrics could detect BOS with an accuracy of 85%. However, they only extracted conventional CT parameters instead of radiomic features and assessed only a single SVM model. Compared with CT, 18F-FDG PET could reveal more metabolic information from lung grafts. However, no study has yet reported the performance of ML-based PET radiomics for the prediction of lung AR.

Before a clinical investigation, the animal model should be placed in an important position. An excellent animal model of LTx should reach the advantages of easy mastery, expeditiousness, low complication rate, and high success rate. In 1989, Mizuta and colleagues innovatively proposed the cuff technique for rat LTx [53]. Based on their cuff technique, some modifications and improvements have been reported in the following three decades [54-58]. Previous publications have not solved the difficulties of the cuff technique model and often require a long learning curve. After the technique practice, most of the performers can master the skill. However, knowing how to do and doing well are completely different concepts. Moreover, intraoperative and postoperative complications still cannot control in previous techniques [56, 59]. To modify the devices and procedures for this technique may shorten and simplify complex steps, thereby encouraging the performer to master it well.

1.6 Specific aims of the study

This study investigated the noninvasive method of AR detection using ML-based 18F-

FDG PET radiomics in a modified rat lung transplantation model and had two main aims:

(1) To propose modifications of orthotopic LTx in a rat model, which achieved the advantages of easy mastery, expeditiousness, low complication rate, and high success rate.

(2) To construct ML-based PET radiomics models for predicting AR and evaluate their potential for further prediction of AR in comparison with SUV_{max} in a rat model.

Chapter 2: Rat lung transplantation model: modifications of the cuff technique

2.1 Introduction

The cuff technique of the rat lung transplantation (LTx) model was first reported by Mizuta et al. in 1989 [53]. Recently, various modifications and improvements have been reported [54-57]. Although it has been thought that any trained surgeon could perform this technique successfully, the difficulties and disadvantages of this model still exist and often require a long learning curve [59]. In addition, complications such as twisted blood vessels, pulmonary atelectasis, bleeding, and thoracic effusion still occur, although some recipient rats survive without any symptoms [56]. Because improper devices and procedures for this technique could lead to frustration and failure to complete one's training, disclosing the improvements of the devices and procedures may shorten and simplify complex steps, thereby encouraging the trainee to continue. This chapter describes the modifications in this cuff technique that optimize the rat LTx model, helping to achieve successful operations in a shorter time with a lower complication rate.

2.2 Methods and material

2.2.1 Devices and instruments

Small, handheld surgical instruments and larger equipment for rat LTx were used as in previous studies of Kyoto University [60, 61]. I have modified the device for cuff preparation and used a petri dish attached to two foam blocks. A groove and hole were carved on the foam blocks to match the ends of a bulldog clamp **(Figure 1A)**. To prevent lung tissue injury, I modified the ends of the cuff tail to round **(Figure 1B).**
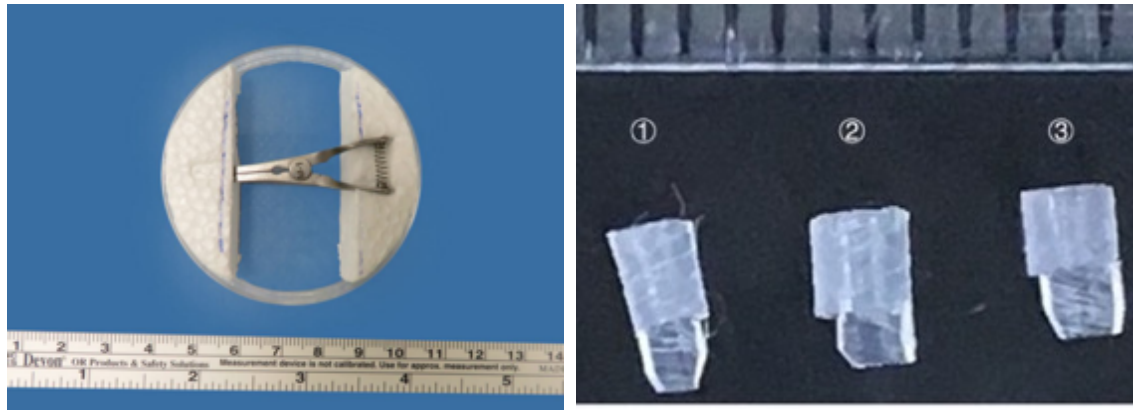
Figure 1: Hand-made instruments.
Cuff preparation dish. A groove and hole were carved on the foam blocks to match the ends of a bulldog clamp (**A**). Modified cuff for hilar structures. The ends of cuff tail were modified from rectangular to round (**B**).

2.2.2 Animals

Male Brown Norway and Lewis rats were purchased from Japan SLC, Inc. (Hamamatsu, Japan). Models of syngeneic and allogeneic transplantation were performed as described previously [60]. Briefly, for allogeneic transplant, nine- to ten-week-old Brown Norway weighing about 250g are used as donors, and eleven- to twelve-week-old Lewis weighing 300g are used as recipients. For syngeneic transplant, Lewis rats are used as both donors and recipients. Allogeneic LTx recipients were subcutaneously administered 25 mg/kg CsA (Novartis pharma, Tokyo, Japan) on four days in the first week. All recipients were executed 0.5g/Kg Cefazolin sodium (Nichi-Iko Pharmaceutical Co, Toyama, Japan), 30mg/Kg Methylprednisolone Sodium Succinate (Pfizer, Tokyo, Japan), and 10mg/Kg Furosemide (Teva Takeda Pharma Ltd, Aichi, Japan) at postoperative day one and day two. Animals were sacrificed at ≥2 weeks postoperatively. All rats were maintained under specific pathogen-free conditions at the Life Science Research Building of The University of Tokyo. Animals were fed a standard diet and provided with water ad libitum. This study was approved by the Experimental Animal Ethics Committee of The University of

Tokyo (No. H19-027). All procedures were performed in accordance with the guidelines

of the Institutional Animal Care and Use Committee at The University of Tokyo.

2.2.3 Time-interval definitions

The donor operation time was the interval from the incision of the donor rat to excision

of the heart–lung block. The cuff preparation time was the interval from excision of the

heart–lung block to completion of cuff placement. The cold ischemia time was defined at

the time from flushing the donor lungs in situ with ET-Kyoto solution (Otsuka, Tokushima,

Japan) to graft removal from hypothermic storage. The warm ischemia time was set as

the interval from donor lung removal from the ice until the restoration of the reperfusion.

The total procedure time was the interval from the donor's skin incision until the closure
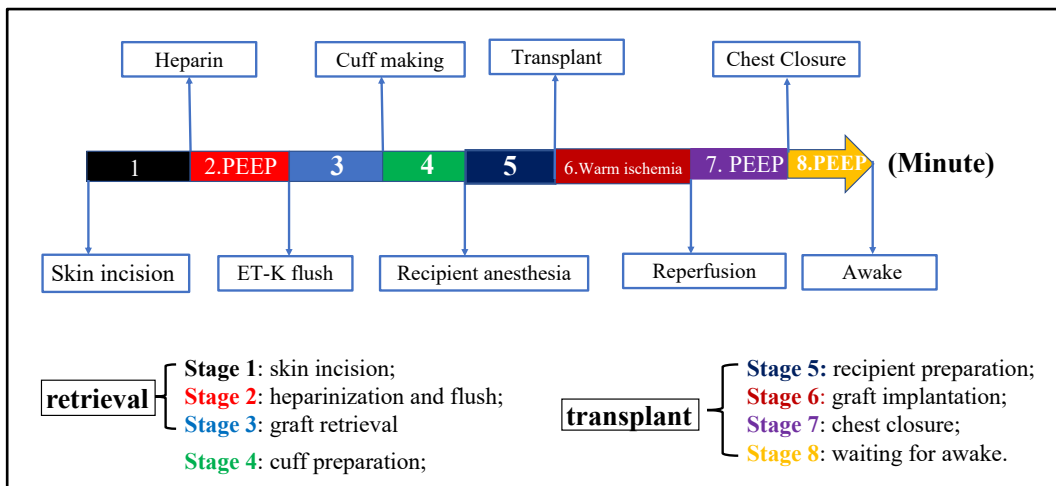
of the recipient's incision (**Figure 2**).

Figure 2: Time-interval definitions.
Donor operation time: Stage 1-3; Cuff preparation time: Stage 4; Cold ischemia time:
Stage 3-5; Warm ischemia time: Stage 6; Total procedure time: Stage 1-7.

2.2.4 Donor procedures

Donor heart–lung block retrieval was performed as in previous studies [60, 61]. The detailed procedures are displayed in **Figure 3**. All rats were performed by oral intubation on a hand-made curved metal plate. The parameter of gas anesthesia was set as follows; sevoflurane 5% for induction and 3% for maintenance with a ventilator (FiO$_2$ 0.21, TV 10ml/kg, RR 80bpm, PEEP 0-3 cmH$_2$O). After the hilar structures of the left main bronchus, pulmonary artery (PA), and pulmonary vein (PV) with part of the left atrium were dissected (**Figure 4A**), the hilar structures were consecutively everted around the cuff and secured by a preparatory 6-0 slipknot (**Figure 4B**). The graft was rewrapped by organ perfusate-soaked paper and stored on ice for implantation (**Figure 4C**).
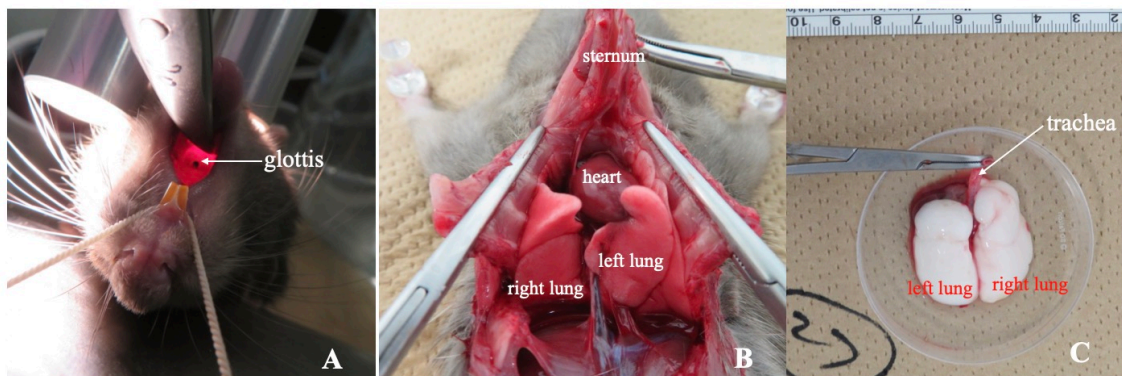

Figure 3: Donor heart–lung block retrieval.
Expose the glottis for oral intubation (**A**); Parasternotomy to expose donor heart–lung block (**B**); Heart–lung block retrieval (**C**).
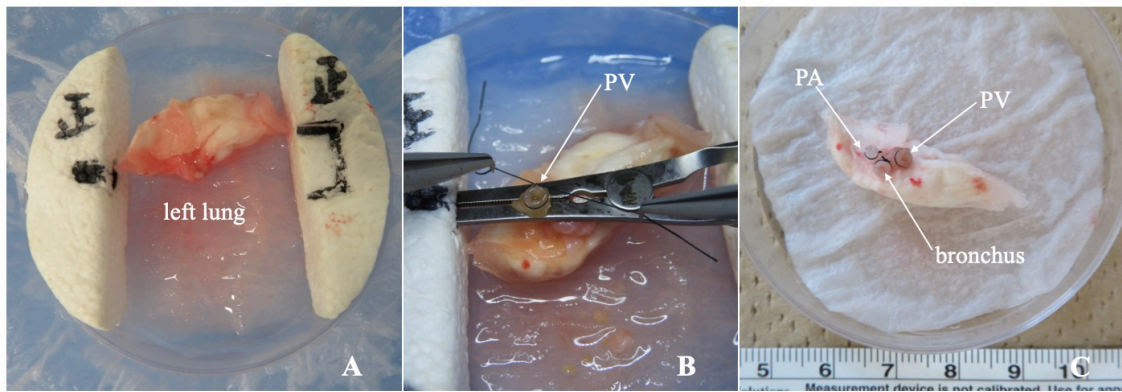
Figure 4: Cuff preparation.
Left lung graft (**A**); The PV were everted around the cuff and secured by a preparatory 6-0 slipknot (B); Three hilar structures were prepared by cuff technique (**C**).

2.2.5 Recipient procedures

A thoracotomy incision was made from the area of a palpable cardiac impulse on the chest wall and extended dorsally for about 3–4 cm (**Figure 5A**). A blepharostat was used as a chest retractor (Speculum BANGERTER Large Right; Inami, Tokyo, Japan) to expose the thoracic cavity (**Figure 5B**). The hilar structures were dissected and then clamped distally and proximally using two Satinsky clamps (**Figure 5C**). The Satinsky clamps were then fixed in plastic clay to place mild tension on the bronchovascular structures. A "⊥"-shaped incision was made on the front wall of PA using microscissors. "V"-shaped incisions were made from inferior-to-superior branches of PV and bronchus (**Figure 6**).
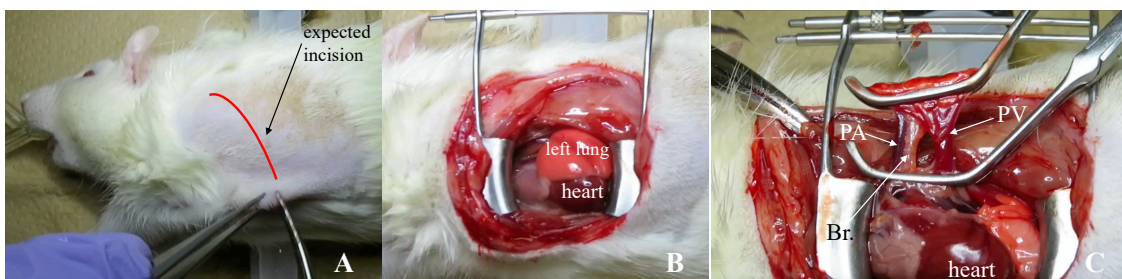

Figure 5: Recipient procedures.
Incision location (**A**); Expose the thoracic cavity (**B**); hilar structures dissection (**C**).
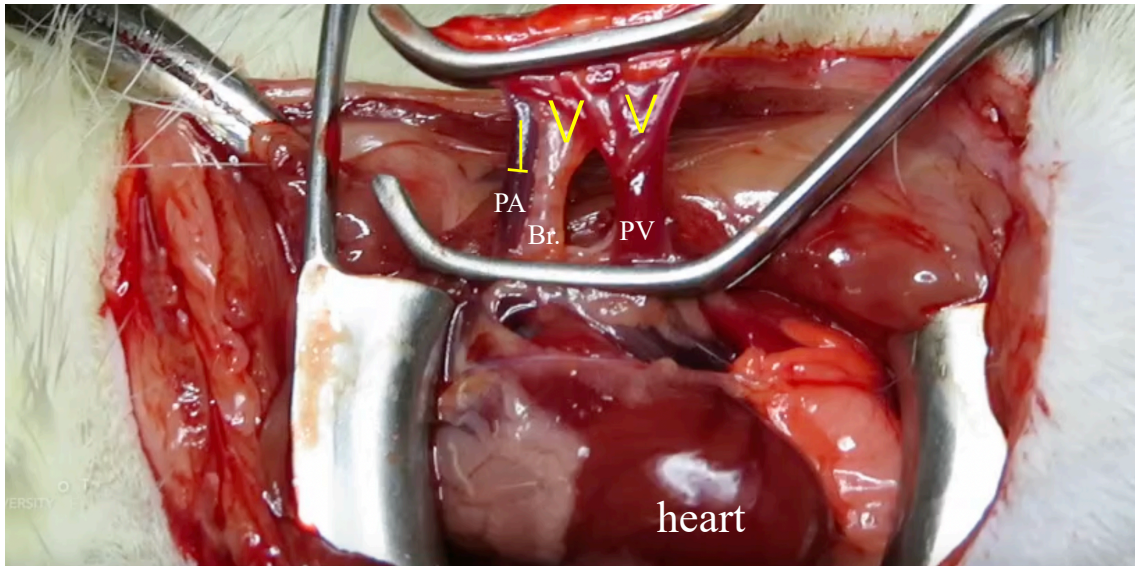PA: pulmonary artery; Br.: bronchus; PV: pulmonary vein.

Figure 6: Incisions on the hilar structures.
⊥-shaped incision was made on the front wall of the PA using micro-scissors. V-shaped incisions were made from the inferior-to-superior branches of PV and bronchus.
PA: pulmonary artery; Br.: bronchus; PV: pulmonary vein.

Here, I first proposed the "pendulum model" method for implantation. Briefly, the bronchus was implanted first. The native bronchus and cuff body were secured using a preparatory 6-0 nylon knot positioned loosely around the recipient bronchus. The superior bifurcation of the bronchus was excised to eliminate any overlaps between the bronchus and the PA. The donor lung was then repositioned to allow a PA anastomosis without tension. The donor lung was repositioned again to allow the creation of the PV anastomosis without tension. The PA and PV were implanted in an analogous fashion as with the bronchus **(Figure 7)**. After excising the left native lung parenchyma, the end rim of the native structures was cut for debonding before reperfusion **(Figure 8)**.
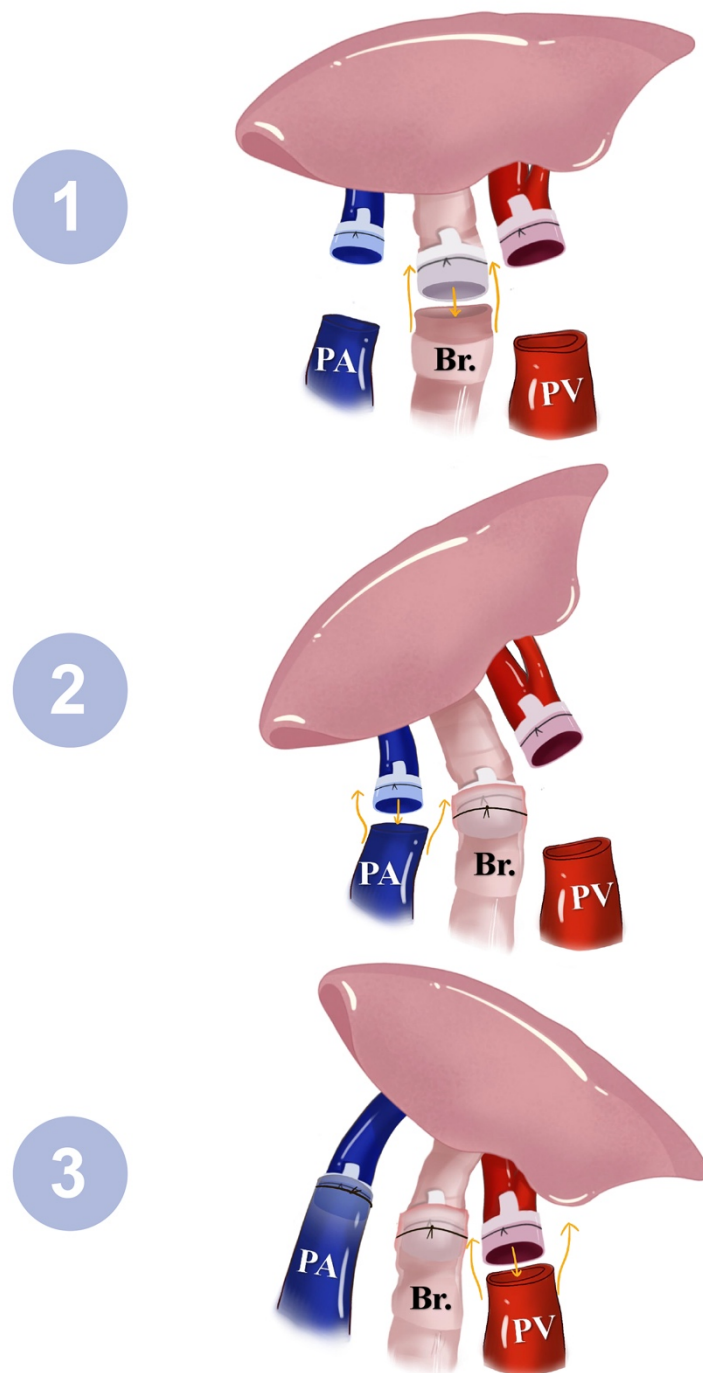
Figure 7: The "pendulum model" for hilar structures implantation.
The bronchus was implanted and secured using a preparatory 6-0 nylon around the recipient bronchus. The graft was then repositioned to allow a PA anastomosis without tension. The donor lung was repositioned again to allow the creation of the PV anastomosis without tension. PA: pulmonary artery; Br.: bronchus; PV: pulmonary vein.
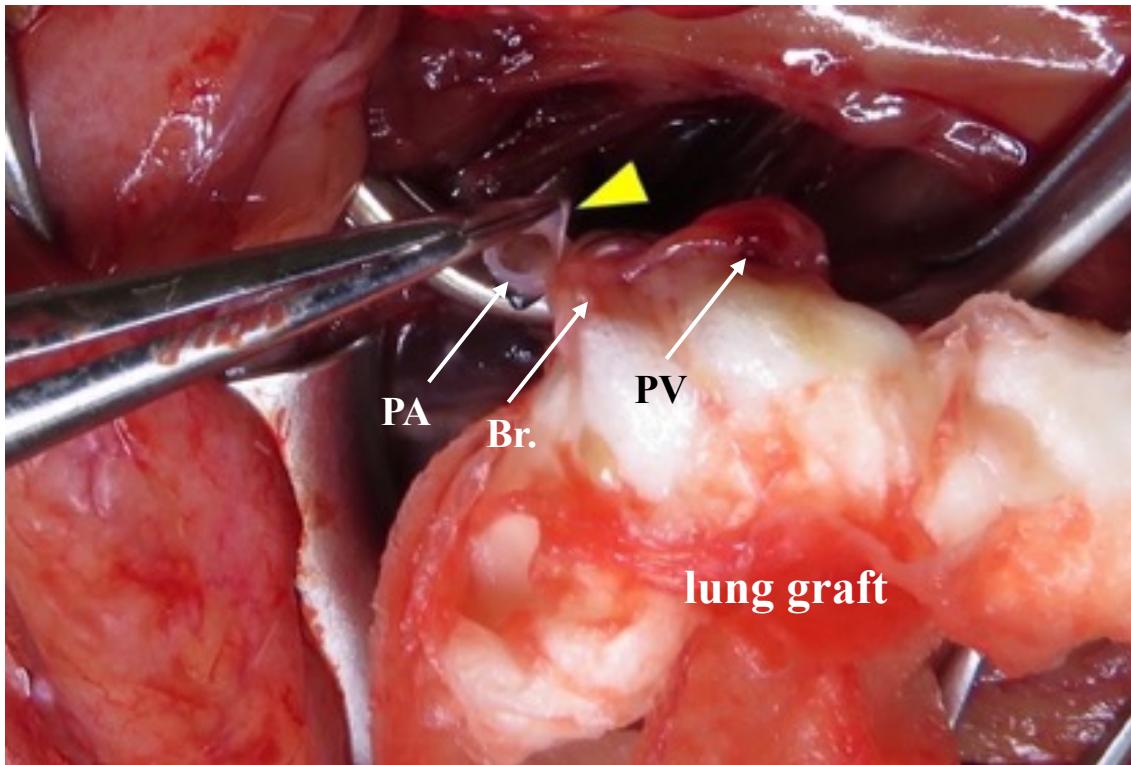
Figure 8: End rim of the native structures.
The end rim of native structures was cut for debonding before reperfusion (yellow ▽).

2.2.6 Assessment of chest-radiography and histology

Post-transplantation rats underwent chest plain radiography on postoperative day 7 to screen for complications such as atelectasis or recorded complications at the time of sacrifice. For routine histological evaluation, lung grafts were fixed in 10% formalin, embedded in paraffin, sectioned into 4-μm thickness, and stained with hematoxylin-eosin.

2.2.7 Statistical analysis

Results were expressed as means ± SD. The results were analyzed by SPSS 24.0 software (IBM, Armonk, NY, USA).

2.3 Results

2.3.1 Key tricks and modifications on techniques and devices

The following devices and techniques were improved and modified **(Table 1)**.

(1) Regarding the devices, I modified the cuff preparation plate, which now contains a petri dish attached to two foam blocks. A groove and hole were carved on the foam blocks to match the ends of a bulldog clamp. This modified plate stabilized the operation, was less injurious, and made the procedure easier to master.

(2) When locating the incision site on the recipient, the region of apical impulse, or palpable cardiac impulse on the chest wall, was first confirmed and then extended dorsally for about 3–4 cm. This position was located more easily and was suitable for the following implantation. Before implantation, a "⊥"-shaped incision was made on the PA, and "V"-shaped incisions were made on the PV and bronchus. These improvements made implantation easier and lacerations on the structures less likely to occur.

(3) The "pendulum model" method was used for implantation. First, the bronchus was implanted. Thereafter, the donor lung was repositioned to close the PA and PV, thereby allowing a tension-free anastomosis. In addition, I modified the cuff with a round tail, used the slip-knots for cuff preparation, and debonded the end rim of the native structures after implantation.

Table 1: Key tricks and modifications on techniques and devices

Items	Previous status	Modifications	Advantages
Preparation plate	Petri dish only	Two foam blocks with a petri dish (Figure 1)	Keep stable, cause less injury, easy to master
Cuff	Rectangular tail	Round tail (Figure 2)	Prevent accidental injury
Recipient thoracotomy	3rd/4th Intercostal space	Region of the apical impulse	Easily confirm the correct skin site for the incision
Hilum structure incisions	Transverse or ⊢- shaped incision on the front wall	(1) ⊥ -shaped incision for PA (2) V-shaped incisions on the bifurcations of the PV and bronchus (Figure 3)	(1) Prevent laceration of pulmonary artery (2) Easily implanted and free of laceration
Implantation	Single direction with PV or PA first	"Pendulum model" for implantation	Easy for implantation
Reperfusion	No record	Cut the end rim of native structures (Figure 4)	Prevent compression after reflation and reperfusion

PA: pulmonary artery; PV: pulmonary vein.

2.3.2 Outcomes of rat LTx

In a consecutive series, 180 (syngeneic 33, allogeneic 147) anastomoses were completed without lacerations, twisting, or angulation of intraoperative bronchovascular structures and without bleeding at the vascular anastomosis. There were no intraoperative deaths,

pneumothorax, or vessel thromboses. Partial or complete pulmonary atelectasis was observed in 10 cases (5.6%). Five deaths (2.8%) were found at a follow-up time of 3–7 days, most likely due to pleural effusion.

2.3.3 Operation time of rat LTx of all procedures

The mean weights of the rats at the time of transplant of Lewis and Brown Norway rats were 239.7 ±42.8 g and 291.2 ±23.0 g, respectively. The mean operative times of heart-lung block retrieval, cuff preparation, cold ischemia, warm ischemia, and total procedure time are seen in **Table 2**.

Table 2: Overall operative time for rat lung transplantation

Single procedure	Operative time (min)
Heart-lung block retrieval	8.4±0.8
Cuff preparation	8.1±1.4
Cold ischemia	26.4±2.2
Warm ischemia	8.1±1.2
Total procedure	48.0±2.8

• Heart–lung block retrieval: from the incision on donor rat to excision of heart–lung block.
• Cuff preparation: from excision of left donor lung to completion of cuff placement.
• Cold ischemia: from flushing the donor lungs in situ with ET-Kyoto solution to graft removal from hypothermia storage.
• Warm ischemia: from donor lung removal from ice until the restoration of reperfusion.
• Total procedure: From donor skin incision until the closure of the recipient incision.

2.4 Discussion

Although several studies have introduced technical modifications for rodent LTx after Mizuta and colleagues first reported the cuff technique [53], some critical and challenging key procedures have not been described. Rat LTx remains a difficult procedure, necessitating a long learning curve. In this study, I modified the operative devices and the cuff techniques to make it easier to master the procedure with a low complication rate and a high success rate. Because it is a more expeditious operation, the ischemic times were shorter than those in a previous study [53] with fewer complications and no intraoperative deaths.

Only a few studies have reported on the instruments used for cuff preparation, although instruments can determine the success of this technique in the rat LTx model. Sugimoto et al. [62] used a petri dish for cuff preparation. With their technique, the donor lung was compressed and unstable when the cuff was created. A previous study reported the cuff preparation time at 18.7 minutes, which is more than twice my technique [57]. I introduced a modified cuff preparation plate to stabilize the cuff preparation, make it easier to master and more expeditious. With this improved device, the cuff preparation time was only 8.1 min, with no structural lacerations in my series.

The skin incision of the recipient is important for transplantation. It is impossible to measure the intercostal space on a rat before surgery. However, most previous reports that described the incision location relied on different intercostal spaces [55-57, 59, 63, 64]. Habertheuer et al. [65] started the skin incision 1 cm below the inferior margin of the scapula, which is unreliable because the scapula is easily mobilized. In this series, I

located the region of palpable cardiac impulse on the chest wall. This apical impulse region is at the third or fourth intercostal space level, as previously described [56, 59, 64, 66]. However, it seems more valuable to follow this apical impulse when performing rat LTx. This series showed no failures in placing a suitable incision.

Another key trick is to locate the incisions on the recipient's PV, bronchus, and PA. An expeditious technique is essential to shorten the warm ischemia period and minimize pulmonary injury. Most of the previous reports made a transverse incision on the front wall of the recipient's hilar structures [55, 62, 65, 67, 68]. Guo et al. [57]made the incision in a " ├" shape toward all the structures. Jungraithmayr et al. [69] made the incision on the lower branch of the PV. I first introduced the "V"-shaped incisions from the inferior-to-superior branches on the PV and bronchus cuffs. This "V"-shaped incision follows a wide rim of structure ostium, which allows the donor graft to be easily implanted without laceration. To match the lengths of the Br and PV, the "⊥"-shaped incision is made on the front wall of the PA, which can well prevent proximal laceration at implantation. Guo et al. [57] reported a 5% intraoperative failure rate of their technique due to bleeding and pulmonary vein injury during the operation. This study showed no intraoperative failures with hilar structure lacerations.

The "pendulum" model for implantation was proposed in this study. Previous investigators often chose vessels as the first step. Rajab et al. [64] addressed PV first, followed sequentially with the bronchus and PA. Sugimoto et al. [62] went in the opposite direction, with the PA, bronchus, and PV, respectively. In this study, I anastomosed the bronchus first because, compared with vessels, it is structurally solid and easy to

anastomose without laceration. In addition, I cut the superior bifurcation of the bronchus before the PA anastomosis because the bronchus and PA are always located adjacent to each other. Previous studies have not been concerned about the rim of the native hilum structures before reperfusion. Because the rim of the structures may contract and compress the graft structures, I cut the rim of the native structures to release them. With this technique, no vessel thrombosis, inadequate blood supply, or airway compression occurred after reperfusion and reinflation. Regarding the implantation time, previous studies reported an implantation time (warm ischemia time) of 15.2–20.0 min [57, 59, 65]. The warm ischemia time was only 8.1 min with this modified implantation technique.

Previous studies also showed follow-up survival rates of < 90%. The intraoperative deaths were mainly due to pleural effusion, venous cuff failure, or pyothorax [53, 57, 65]. Habertheuer et al. [65] reported about 18.9% of cases were lost because of severe pleural effusions during the postoperative period. With this approach, the total follow-up survival rate was 97.2% (175/180), with no intraoperative deaths. A high success rate not only saves cost and time, but can also strengthen the operator's confidence during surgery. All five deaths in this study were most likely due to pleural effusion. Minor bleeding from intercostal muscles is difficult to detect and may have caused pleural effusion. As effusion accumulates, it may compress the grafted lung, causing a life-threatening complication. Thus, careful inspection is necessary before chest closure.

Pulmonary atelectasis is a common, severe complication of rat LTx. Although a rat can survive without apparent symptoms, the animal may not be used for further evaluation. In this study, only 5.6% of rats experienced graft atelectasis during the follow-up period,

which appears to be an acceptable result for the rat LTx model. In this series, the post-LTx complications and follow-up deaths were rare. Reperfusion injury, a significant cause of graft injury, is related to the ischemia time. A decrease in reperfusion pressure is thought to minimize this complication [70-72].

2.5 Conclusions

I developed modifications of devices and procedures of the cuff technique for the rat LTx model. The advantages of this modified cuff technique include its expeditiousness, low complication rate, and high success rate. These improvements could further facilitate rat LTx in a feasible, reproducible manner.

Chapter 3: Noninvasive monitoring of allograft rejection in a rat lung transplant model: Application of machine learning-based 18F- fluorodeoxyglucose positron emission tomography radiomics

3.1 Introduction

Although lung transplantation (LTx) is the optimal treatment for end-stage lung diseases [73], allograft rejection (AR) is a significant complication limiting patient survival after LTx, even though new and effective immunosuppressive drugs have been introduced [74, 75]. AR involves a change that develops silently without apparent symptoms. Timely diagnosis of AR is crucial for allograft function and a good prognosis of LTx [76]. Currently, lung biopsy is the only method that can accurately diagnose AR. However, biopsy can damage the lung graft and is regarded as a contraindication in patients taking anticoagulant treatment. Moreover, the limited sampling of tissue biopsies may lead to false-negative results [77]. Therefore, there is an ongoing search for new noninvasive strategies to diagnose AR [78].

18F-fluorodeoxyglucose (18F-FDG) positron emission tomography (PET) has the potential to be more effective than common imaging modalities when applied to organ transplants because changes in graft metabolism commonly occur before anatomical changes [33, 79]. However, only scattered studies have described PET as a noninvasive approach for quantifying lung AR. Findings from Chen and colleagues [44] revealed that increased T-cell glucose uptake reflected AR in lung grafts which was potentially assessed by 18F-FDG PET. Moreover, standardized uptake values (SUVs) derived from 18F-FDG PET were demonstrated to be valuable quantitative measurements with good

detective ability for lung AR [44, 45]. Recently, in fields other than AR, accumulating evidence has shown that radiomics, a noninvasive advanced imaging analysis method, typically has high accuracy in disease diagnosis and is effective for evaluating treatments [47, 48]. Radiomics is a new and developing field in medical imaging and can quantify spatial relationships among image voxels with the aim of relating imaging information to clinical outcomes. Because of its high-dimensional nature (which seems to be ever-growing as research continues), the field of radiomics needs powerful analytical tools. Machine learning (ML), a branch of artificial intelligence, appears to be a potential candidate for this purpose, having shown powerful capabilities in radiological research [50]. Currently, studies reporting the use of ML algorithms for the detection of lung AR are low in number [51, 52], and no study has yet reported the performance of ML-based PET radiomics for monitoring lung AR.

Using a rat LTx model, I extracted the maximum standardized uptake value (SUV_{max}) and radiomic features from regions of interest (ROIs) in PET images. I evaluated correlations between the pathological results and the SUV max and radiomics score (Rad-score), with this latter value being calculated from selected radiomic features. I used eight modeling algorithms (seven ML algorithms and one logistic regression [LR]), with six feature selection methods to construct 48 radiomics models for monitoring AR, and evaluated their potential for further monitoring of AR in comparison with the SUV_{max}.

3.2 Materials and methods

3.2.1 Animals and the orthotopic left LTx model

This study was approved under license number H19-027 from the Experimental Animal Ethics Committee of The University of Tokyo. All procedures complied with the Institutional Animal Care and Use Committee guidelines at The University of Tokyo. Male Brown-Norway rats aged 8–10 weeks and male Lewis rats aged 10–12 weeks were purchased from Japan SLC, Inc. (Hamamatsu, Japan). I used the "pendulum" rat LTx model, which I reported previously for this study [80]. All rats were performed by oral intubation on a hand-made curved metal plate. The parameter of gas anesthesia was set as follows; sevoflurane 5% for induction and 3% for maintenance with a ventilator (FiO_2 0.21, TV 10ml/kg, RR 80bpm, PEEP 0-3 cmH_2O). All rats were fed ad libitum and maintained under specific pathogen-free conditions for the first week post-transplant. A week after transplant, all rats were kept in a conventional room for further PET examinations. Allogeneic and syngeneic transplantation models were performed as in previous literature [80]. Briefly, for the allogeneic model, the Brown-Norway rats and Lewis rats were used as donors and recipients, respectively. The allogeneic recipients were subcutaneously administered 25 mg/kg cyclosporine (CsA; Novartis Pharma, Tokyo, Japan) on post-transplant days 1, 2, 4, and 7. Lewis rats were used for the syngeneic model as both donors and recipients.

3.2.2 Treatment protocols in different groups

The treatment protocols are summarized in **Figure 1.** In brief, rats in the isograft group (n = 8) received no immunosuppressive drugs after LTx. In the allograft-cyclosporine$_{continuous}$ (CsA_{cont}) group (n = 8), rats were subcutaneously administered CsA

until the study endpoint. In the allograft-CsA$_{1week}$ group (n = 8), CsA administration was ceased after the first week. In the allograft-CsA$_{delayed}$ group (n = 4), CsA administration was ceased after the first week but then recommenced after three weeks. Due to the same protocol being processed for the allograft-CsA$_{delayed}$ group and allograft-CsA$_{1week}$ group in the first three weeks, I only set the time point for the allograft- CsA$_{1week}$ group at week 3. The allograft-CsA$_{delayed}$ group was developed to achieve the following aims. First, to mimic the clinical situation of the therapeutic process for AR. Second, to dynamically monitor the therapeutic effect on AR by PET prior to and after recommenced CsA therapy. Third, to further confirm the existence of AR at week 3 in both the allograft-CsA$_{delayed}$ group and allograft-CsA$_{1week}$ group. Because immunosuppression therapy is effective for AR but not the infection. Each rat underwent PET scanning only once at week 3 or 6 and was sacrificed for histopathology subsequently. The PET images, along with corresponding histopathological results were included in the following analysis.
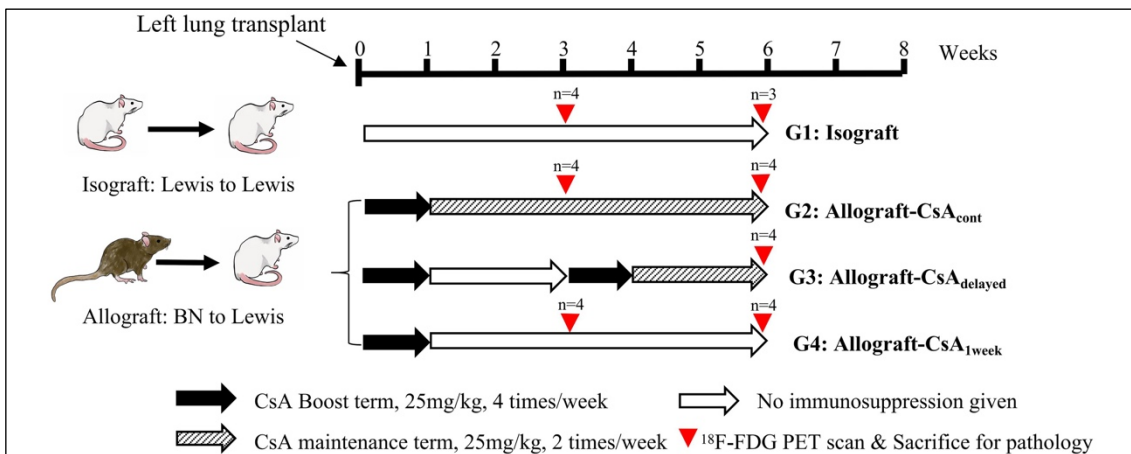

Figure 1: Treatment protocols in the different groups.
Isograft: No immunosuppressive drugs (CsA) after LTx.
Allograft-CsA$_{cont}$: CsA administered twice-weekly until the endpoint.
Allograft-CsA$_{1week}$: CsA administration was ceased after the first week.
Allograft-CsA$_{delayed}$: CsA administration was ceased after the first week then recommenced after the third week. CsA, cyclosporine; 18F-FDG, 18F-fluorodeoxyglucose; PET, positron emission tomography.

3.2.3 Histopathological evaluation

After 18F-FDG PET scanning, a pre-set number of rats in each group were sacrificed, and the transplanted grafts were retrieved and fixed in formalin overnight. Serial 4-μm tissue sections were stained with hematoxylin-eosin (HE) and Masson's trichrome (MT) stains. Histopathological evaluation was performed according to the AR criteria for A- and B-grade rejections formulated by the International Society for Heart and Lung Transplantation [81] as previously reported and briefly described in **Table 1**. The AR criteria were scored for five random HE-stained slides observed at 100× magnification. Because of overlapping rejection features in the rat LTx model, acute rejection and chronic rejection are not readily discriminated by a fixed time point. Therefore, I used ImageJ version 1.49 (National Institutes of Health, Bethesda, MD) to evaluate the percentage of parenchymal fibrosis [Fibrosis-(%)] to represent the possible level of chronic rejection, in addition to estimating A- and B-grade rejection. The Fibrosis-(%) was also scored for five random slides observed at 100× magnification. One pathologist and one thoracic surgeon performed the evaluations in a blinded manner and discussed conflicting results to reach a consensus. According to the histopathological results, AR was defined as an A- or B-grade rejection score ≥ 1.

Table 1. Classification and grading of pulmonary allograft rejection.

A:	Acute rejection (perivascular mononuclear cell infiltrates)
	Grade 0—none
	Grade 1—minimal
	Grade 2—mild

Grade 3—moderate

Grade 4—Severe

B: Airway inflammation (lymphocytic bronchitis and bronchiolitis)

Grade 0—none

Grade 1R—low grade

Grade 2R—high grade

Grade X—ungradeable

C: Chronic airway rejection—obliterative bronchiolitis

0—absent

1—present

D: Chronic vascular rejection—accelerated graft vascular sclerosis

"R" denotes revised grade to avoid confusion with the 1996 scheme.

3.2.4 Imaging acquisition

The rats were fasted for at least 4 hours before undergoing an 18F-FDG PET scan. Each rat was administered 20 MBq (0.54 mCi) 18F-FDG (Nihon Medi-Physics Co., Ltd., Tokyo, Japan) intravenously via the tail vein under anesthesia. After tracer administration, the rats were placed back in their cages for 50 minutes to allow tracer uptake, and then a 20-minute emission scan was acquired using a micro-PET scanner (ClairvivoPET, Shimadzu Corp., Kyoto, Japan), with the rats under 1.5% isoflurane mask-inhalation anesthesia. One experienced nuclear medicine physician and one thoracic surgeon examined all PET images. Images were reconstructed using a 3D iterative dynamic raw-action maximum likelihood algorithm with two iterations, and a 1.4-mm full width at half

maximum Gaussian filter was applied. Attenuation correction was performed using an attenuation map calculated from an emission image.

3.2.5 Image analysis

3.2.5.1 18F-FDG PET quantification

I selected one PET image layer of left lung allograft with highest tracer uptake for delineation using 3D slicer software (Version 4.10.2, https://www.slicer.org). The selected PET images were quantified by drawing an ROI (**Figure 2**). The SUV_{max} was normalized for body weight and injection dose, and a time-decay correction was also performed for the time from injection-dose measurement to the data acquisition. For each rat, one thoracic surgeon and one radiologist defined the ROI on the 18F-FDG PET image and then reached a consensus on the contouring. PET images with various degrees of tracer uptake from all recipient rats were included together for further radiomics analysis.
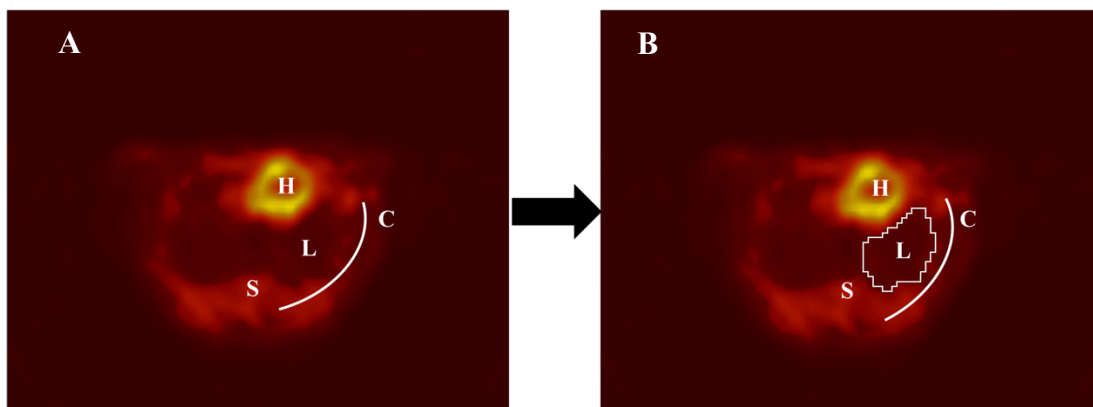

Figure 2: The region of interest delineation process in a rat PET image.
The rat heart (H), spine (S), and left chest wall (C), which are adjacent to the lung (L), often presented higher tracer uptake than the normal pulmonary parenchyma (**A**). Therefore, the border of the lung graft was easily identified and manually delineated the target layer of the left lung allograft that represented the region of interest (**B**).

3.2.5.2 Radiomic feature extraction

Radiomic features were extracted from the ROI using the PyRadiomics package in Python [82]. First-order, gray level co-occurrence matrix, gray level run length matrix, gray level size zone matrix, neighboring gray-tone difference matrix, and gray level dependence matrix features were extracted from the original and wavelet-transformed images. The wavelet-transformed images were derived from the original image using filters with eight frequency band combinations [83].

Full descriptions and mathematical definitions of the radiomic features described above can be found online (https://pyradiomics.readthedocs.io/en/latest/). Min-max normalization was used to preprocess all radiomic features.

3.2.5.3 Radiomics score (Rad-score) calculation

The least absolute shrinkage and selection operator (LASSO) regression, a logistic regression (LR) with an L1 penalty, was used to identify the radiomic features for constructing a Rad-score. The training data of LASSO regression contains all rats at weeks 3 and 6. Five-fold cross-validation was used for penalty parameter tuning. The Rad-score of each rat was calculated from the selected radiomic features, using coefficients weighted according to the results of the LASSO regression.

3.2.5.4 Machine learning models

The models were trained by the radiomic features from all rats for AR classifiers. To avoid overfitting and the curse of dimensionality, six feature-selection methods were used in

the analysis. These methods were divided into three categories: filter methods (distance correlation, information gain), wrapper methods (recursive feature elimination, Boruta algorithm), and embedded methods (random forest [RF], LASSO) [84]. Based on a corresponding score, I selected the top 10 highest-scoring features for the filter methods. For wrapper and embedded methods, all the optimal features were calculated automatically.

Furthermore, one conventional LR and seven ML algorithms (support vector machine, RF, artificial neural network, extreme gradient boosting, k-nearest neighbors, naïve Bayes, and adaptive boosting) were used for fitting AR classifiers. The six subsets of selected radiomic features were used by each of the eight modeling algorithms; hence, a total of 48 models (6*8 = 48) were developed, including 42 ML models (6*7 = 42). I named these models as the names of feature selection and modeling methods.

The performance of these models was assessed using the area under the curves (AUCs) of the receiver operating characteristics (ROC). The optimal model was determined by the AUC value. Additionally, I calculated the AUC on SUV_{max} to compare the optimal model. Decision curve analysis (DCA) was performed to assess the net benefit of SUVmax and the optimal model at different threshold probabilities. The leave-one-out cross-validation (LOOCV) was applied in the performance validation process, as in previous literature [85, 86]. A schematic illustration of the ML-based 18F-FDG PET radiomics for monitoring AR in a rat LTx model is shown in **Figure 3**.
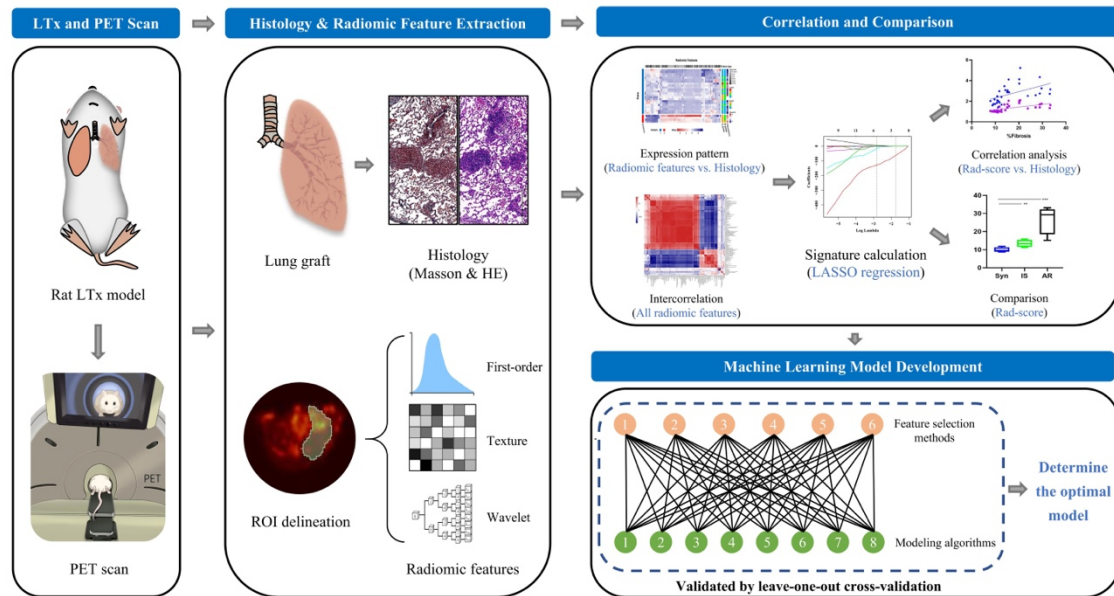
Figure 3: Schematic illustration of machine learning-based 18F-FDG PET radiomics for predicting allograft rejection in a rat lung transplantation model.
18F-FDG, 18F-fluorodeoxyglucose; PET, positron emission tomography; LTx, lung transplantation; ROI, region of interest; HE, hematoxylin-eosin; LR, logistic regression; ANN, artificial neural network; SVM, support vector machine; RF, random forest.

3.2.6 Statistical analysis

Statistical analysis and modeling were conducted using R software (Version: 3.62, https://www.r-project.org/). Quantitative variables are presented as mean ± standard deviation, and categorical variables are presented as number and percent. The SUV_{max} and Rad-score (calculated by the same formula) were evaluated for each group and at each time point (weeks 3 and 6). Spearman's and Pearson's correlation coefficients were used to explore correlations between image parameters (SUV_{max} and Rad-score) and pathological rejection criteria (A-grade, B-grade, and Fibrosis-[%]) in all rat recipients. Unsupervised cluster analysis was performed to examine further connections between the radiomic expression patterns and AR criteria. One-way analysis of variance (ANOVA) with the least-significant difference test and t-tests were used for continuous variables,

while the chi-square test was used for categorical variables. A P-value < 0.05 was considered statistically significant in all analyses.

3.3 Results

3.3.1 Histopathological assessment

All the transplanted rats survived until the endpoint, except one death due to deep anesthesia when scanning in the isograft group at week 3. This rat was excluded from the study. At weeks 3 and 6, the isograft, allograft-CsA$_{cont}$, and allograft-CsA$_{delayed}$ groups showed minimal mononuclear cell infiltration around vessels or bronchioles and no fibrosis, whereas the allograft-CsA$_{1week}$ group showed severe perivascular and interstitial mononuclear cell infiltration, as well as fibrosis around large airways (**Figure 4**).
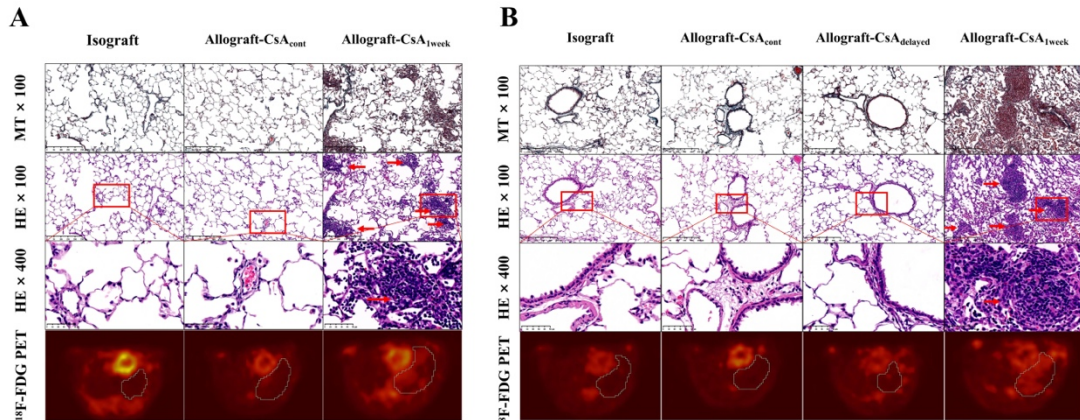

Figure 4: The microscopic findings and ^{18}F-FDG PET images of lung grafts.
The microscopic findings and ^{18}F-FDG PET images are shown for each group at week 3 **(A)** and week 6 **(B)**. At weeks 3 and 6, the isograft, allograft-CsA$_{cont}$, and allograft-CsA$_{delayed}$ groups showed minimal infiltration of mononuclear cells around vessels or bronchioles and almost no evidence of fibrosis, whereas the allograft-CsA$_{1week}$ group showed severe perivascular and interstitial mononuclear cell infiltrates, as well as fibrosis around relatively large airways. The allograft-CsA$_{1week}$ group showed higher tracer uptake than other groups at weeks 3 and 6, corresponding with histopathological results. ^{18}F-FDG, ^{18}F-fluorodeoxyglucose; PET, positron emission tomography; CsA, cyclosporine; MT, Masson's trichrome; HE, hematoxylin-eosin.

At week 3, the allograft-CsA$_{1week}$ group showed significantly worse rejection outcomes than both the isograft and allograft-CsA$_{cont}$ groups according to the AR criteria for A- and B-grade rejection and Fibrosis-(%) (P < 0.05) **(Table 2 and Figures 5A, 5B, 5C)**. At week 6, the allograft-CsA$_{1week}$ group showed significantly higher AR criteria than the isograft group (P < 0.05). Compared with the allograft-CsA$_{delayed}$ group, the allograft-CsA$_{1week}$ group exhibited a higher value in both A-grade rejection and Fibrosis-(%) (P < 0.05). However, B-grade rejection and Fibrosis-(%) in allograft-CsA$_{cont}$ group showed higher value than isograft group at week 6 (P < 0.05) **(Table 3 and Figures 5D, 5E, 5F)**. Furthermore, significant decreases in A-grade rejection and Fibrosis-(%) were found from week 3 to week 6 in the allograft-CsA$_{delayed}$ group (P < 0.05) **(Figure 5G, 5I)**. Although a trend of decreased B-grade rejection was observed in the allograft-CsA$_{delayed}$ group from week 3 to 6, the difference was not significant (P = 0.113) **(Figure 5H)**.

Table 2. Histopathologic AR criteria of the transplanted lung grafts at week 3.

AR Criteria	Isograft	Allograft-CsA$_{cont}$	Allograft-CsA$_{1week}$
A-grade (0/1/2/3/4) †	4/0/0/0/0	2/2/0/0/0	0/1/3/0/0
B-grade (0/1/2) †	4/0/0	3/1/0	0/3/1
Fibrosis-(%) ‡	9.89±1.34	13.39±1.93	26.68±7.94

†: Pathological grades (Stewart et al., J Heart Lung Transplant. 2007; 26: 1229-1242.);
‡: Fibrosis-(%) (Saggar et al., Am J Transplant. 2008; 8: 1921-1930.).
AR, allograft rejection; CsA, Cyclosporine; Fibrosis-(%), percentage of parenchymal fibrosis.

Table 3. Histopathologic AR criteria of the transplanted lung grafts at week 6.

AR Criteria	Isograft	Allograft-CsA$_{cont}$	Allograft-CsA$_{delayed}$	Allograft-CsA$_{1week}$
A-grade (0/1/2/3/4) †	3/0/0/0/0	1/1/2/0/0	2/2/0/0/0	0/0/3/1/0
B-grade (0/1/2) †	3/0/0	1/3/0	2/2/0	0/4/0
Fibrosis-(%) ‡	9.97±1.78	17.10±3.88	11.93±2.60	28.28±3.99

†: Pathological grades (Stewart et al., J Heart Lung Transplant. 2007; 26: 1229-1242.);
‡: Fibrosis-(%) (Saggar et al., Am J Transplant. 2008; 8: 1921-1930.).
AR, allograft rejection; CsA, Cyclosporine; Fibrosis-(%), percentage of parenchymal fibrosis.
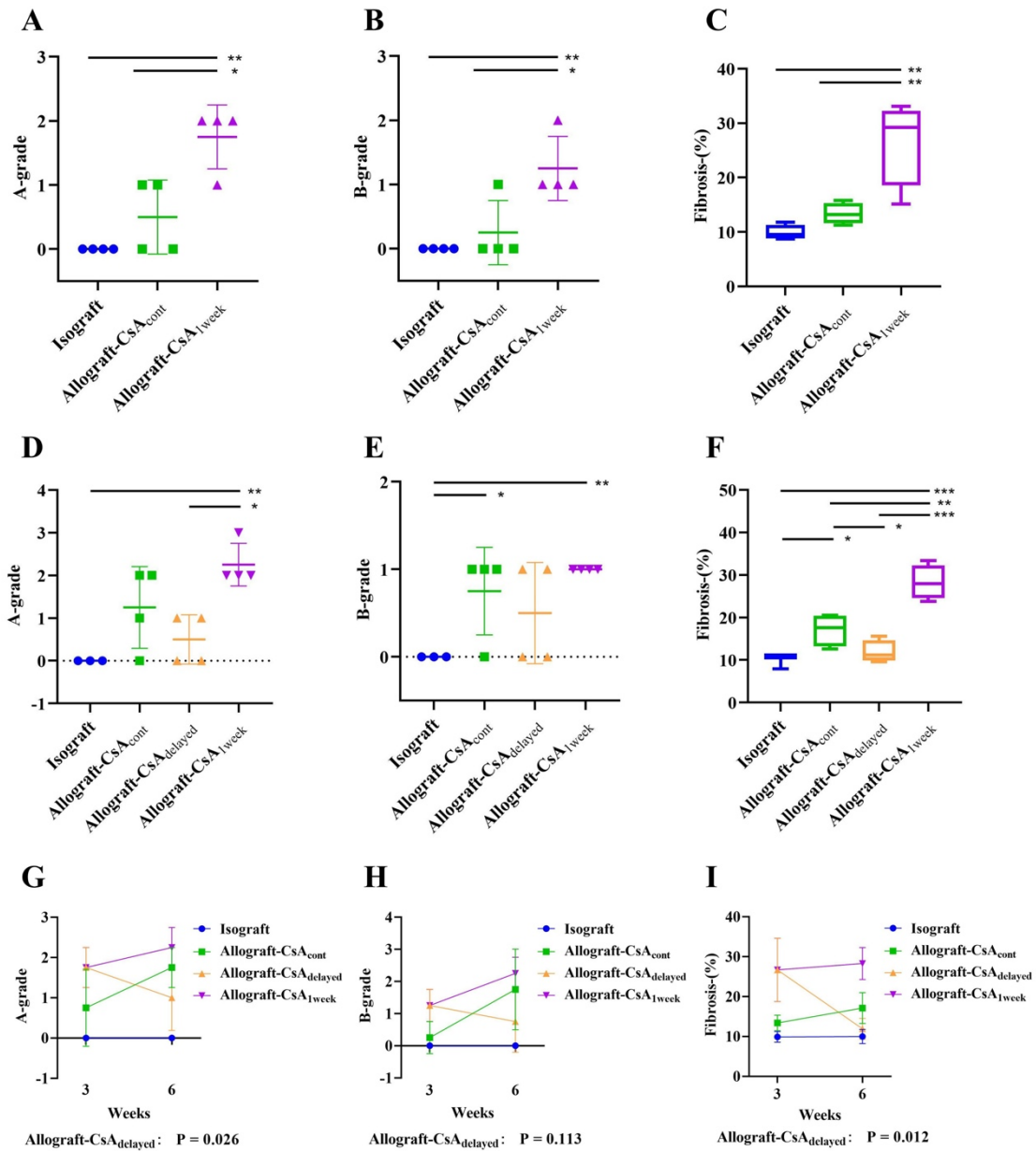
Figure 5: Histopathological assessment on AR criteria of lung grafts.
Histopathologic AR criteria of A- and B-grade rejection and Fibrosis-(%) for each group at week 3 **(A, B, C)** and week 6 **(D, E, F).** Changes in the AR criteria from week 3 to week 6 **(G, H, I)**.

* $P < 0.05$, ** $P < 0.01$, *** $P < 0.001$.

AR, allograft rejection; CsA, Cyclosporine.

3.3.2 Correlations between SUV_{max} and histopathological results

The allograft-CsA$_{1week}$ group showed higher tracer uptake than the other groups at weeks 3 and 6, corresponding with the histopathological results **(Figure 4)**. The SUV_{max} in the allograft-CsA$_{1week}$ group was significantly higher than that in the isograft group (P = 0.011) at week 3 **(Figure 6A)** and significantly higher than those in the isograft (P = 0.002) and allograft-CsA$_{delayed}$ (P = 0.001) groups at week 6 **(Figure 6B)**. In addition, the SUV_{max} in allograft-CsA$_{cont}$ group showed significant higher value than isograft and allograft-CsA$_{delayed}$ group at week 6 (P < 0.05) **(Figure 6B)**. There was a significant decline in SUV_{max} between weeks 3 and 6 in the allograft-CsA$_{delayed}$ group (P = 0.014) **(Figure 6C)**. Pearson's correlation analysis for all recipient rats indicated that SUV_{max} was correlated with the AR criteria of A-grade rejection (r = 0.686, P < 0.001), B-grade rejection (r = 0.573, P = 0.002), and Fibrosis-(%) (r = 0.681, P < 0.001) **(Figure 6D, E, F)**.
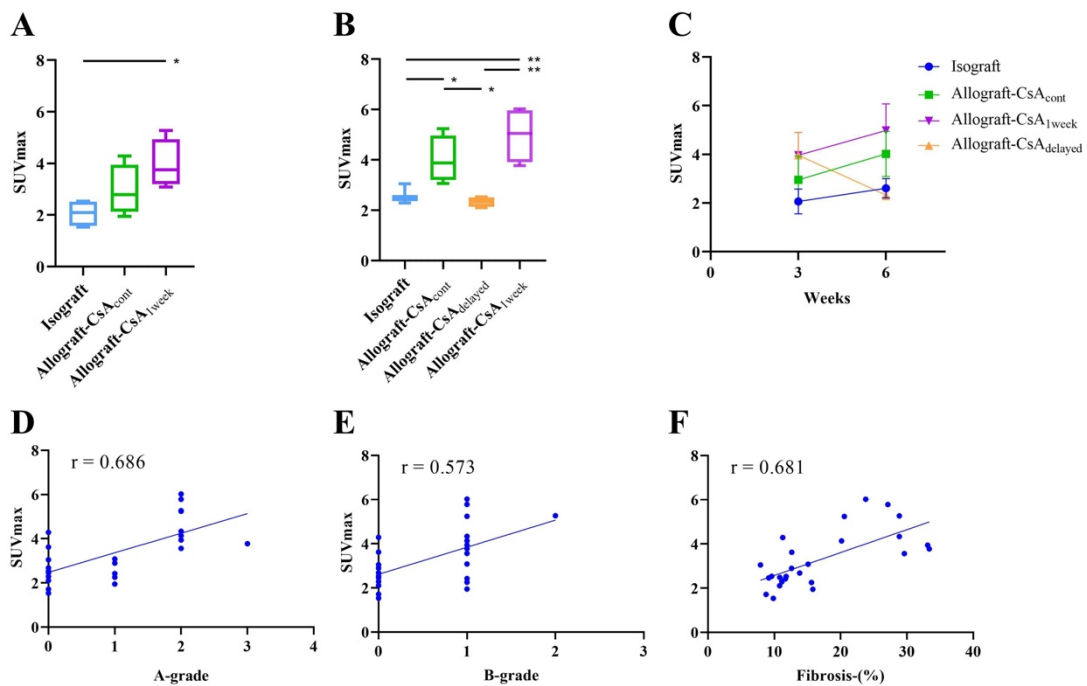

Figure 6: Correlations between SUV_{max} and histopathological AR criteria.
The SUV_{max} of each group at week 3 **(A)**, week 6 **(B)**, and changes in SUV_{max} from week

3 to week 6 (P=0.014) **(C)**.

* P < 0.05, ** P < 0.01, *** P < 0.001

r, Pearson's correlation coefficient; AR, allograft rejection; CsA, Cyclosporine; Fibrosis-(%), percentage of parenchymal fibrosis; SUV$_{max}$, maximum standardized uptake value.

3.3.3 Radiomic feature selection and Rad-score calculation

In total, 837 radiomic features were extracted from each ROI. A large number of radiomic features showed an acceptable correlation with the histopathological results **(Figure 7)**. The internal correlation matrix revealed that most of the 837 extracted radiomic features contained similar information (**Figure 8**). Unsupervised clustering analysis demonstrated two clusters of rats were significantly different in terms of A- and B-grade rejection and Fibrosis-(%) (P = 0.002, 0.007, and 0.027, respectively) (**Figure 9A**).
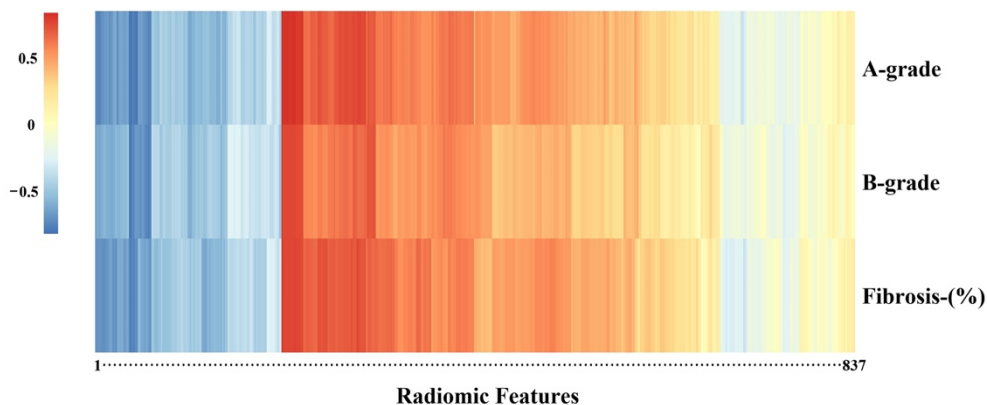

Figure 7: Heat map of the correlations between radiomic features and histopathologic AR criteria.
A large number of the radiomic features and histopathologic AR criteria of A- and B-grade rejection and Fibrosis-(%) were significantly correlated.
A- and B-grade rejection (Stewart et al., J Heart Lung Transplant. 2007; 26: 1229-1242).
Fibrosis-(%) (Saggar et al., Am J Transplant. 2008; 8: 1921-1930).
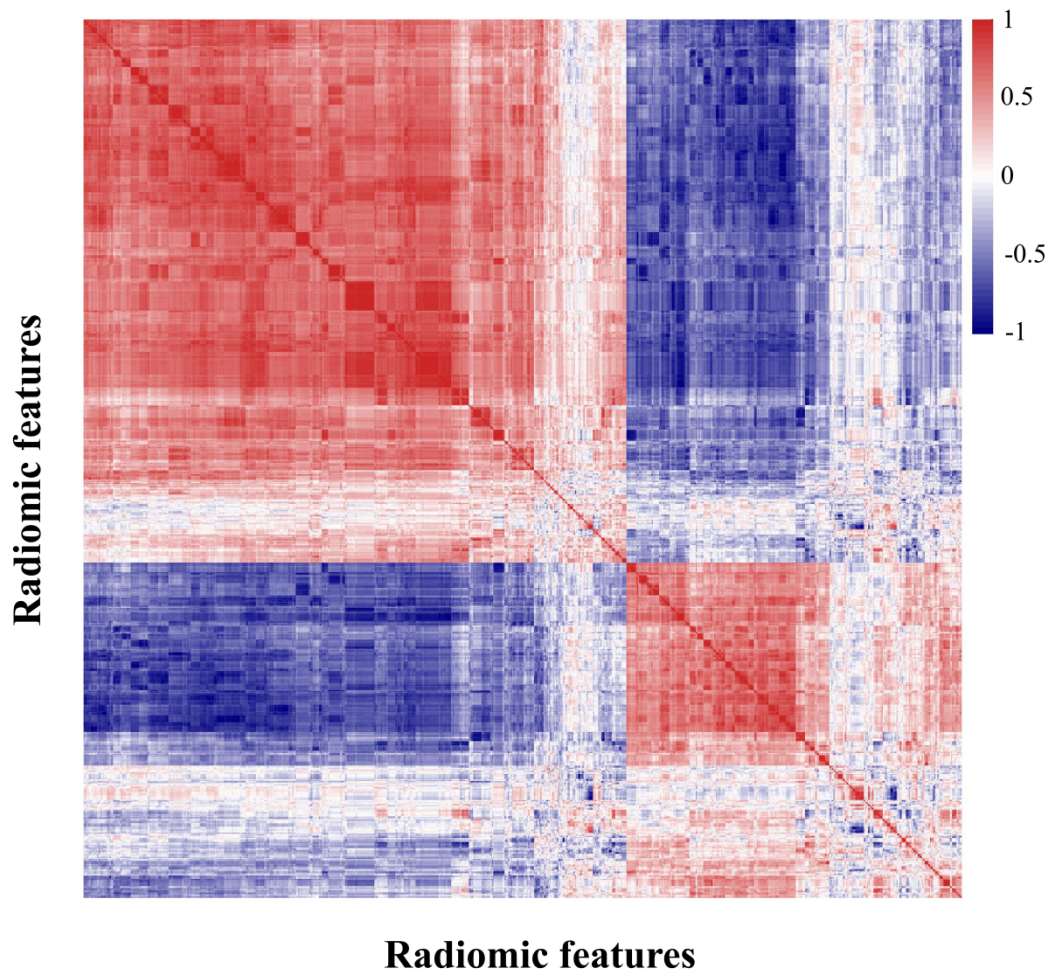AR, allograft rejection; Fibrosis-(%), percentage of parenchymal fibrosis.

Figure 8: Heat map of the internal correlation matrix for the 837 radiomic features. A total of 837 radiomic features were extracted, and most of them represented similar information.

Of all the radiomic features, seven with nonzero coefficients in the LASSO regression were selected as AR-related features: original_GLCM_Informational Measure of Correlation (IMC) 2, original_GLCM_Maximum Probability, original_GLDM_Gray Level Non-Uniformity (GLN), original_GLRLM_Run Variance (RV), original_NGTDM_Busyness, wavelet.LHL_first-order_Median, and wavelet.LLL_GLCM_MCC **(Figures 9B, C)**. The Rad-score for each rat was calculated using these seven AR-related features as follows: Rad-score = 0.29956341 + (0.04668723 × original_GLCM_IMC 2) + (−0.27938774 × original_GLCM_Maximum Probability) +

(−0.41407356 × original_GLDM_GLN) + (−0.04741756 × original_GLRLM_RV) +

(−0.08513070 × original_NGTDM_Busyness) + (−0.32144870 × wavelet.LHL_first-

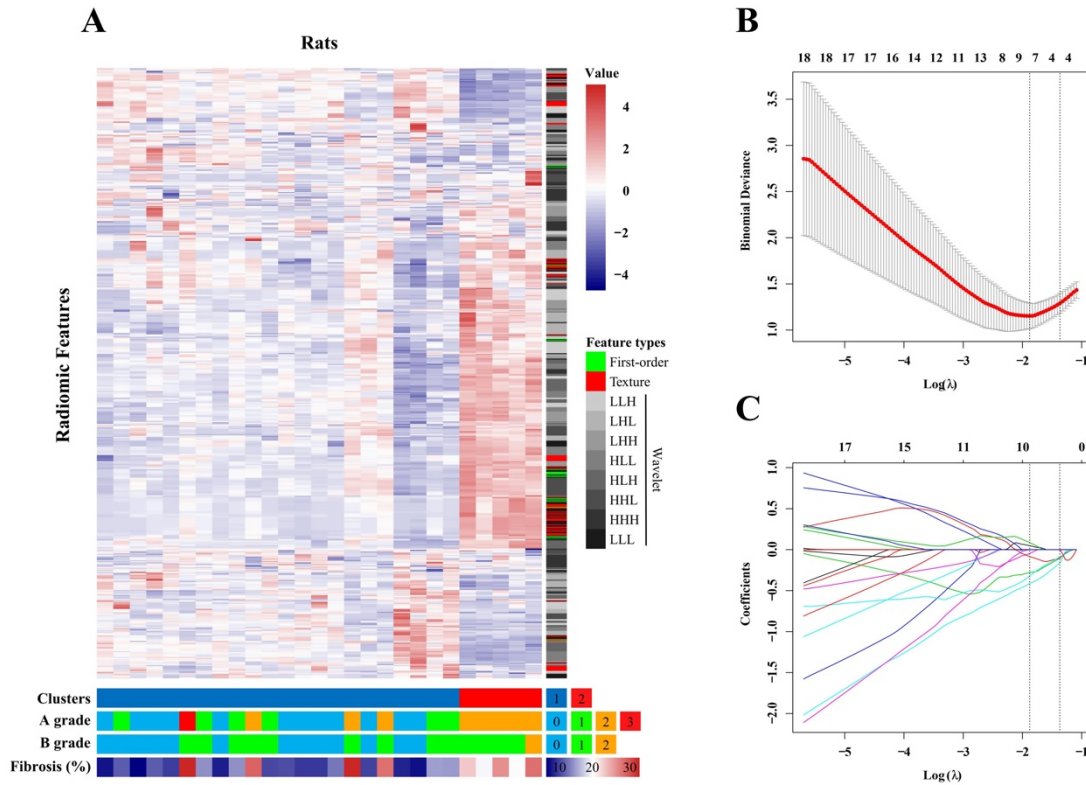order_Median) + (0.08608483 × wavelet.LLL_GLCM_MCC).

Figure 9: Radiomics heat map and feature selection.

A total of 837 radiomic features were extracted.

(A) Unsupervised clustering analysis revealed that radiomic expression patterns were significantly associated with histopathological A-grade (P = 0.002) and B-grade (P = 0.007) AR criteria and Fibrosis-(%) (P = 0.027).

(B) Optimal feature selection according to AUC values. When the value ln (λ) increased to −1.878, the AUC reached a peak corresponding to the optimal number of radiomic features.

(C) LASSO coefficient profiles of the 837 radiomic features. A vertical line was drawn at the value identified by 5-fold cross-validation, at which the optimal λ resulted in seven nonzero coefficients.

AR, allograft rejection; Fibrosis (%), percentage of parenchymal fibrosis; LASSO, least absolute shrinkage and selection operator.

3.3.4 Correlations between Rad-score and histopathology results

At both weeks 3 and 6, the Rad-scores of the allograft-CsA$_{1week}$ group were significantly higher than those of all other groups ($P < 0.05$) except the allograft-CsA$_{cont}$ group at week 6 ($P = 0.138$) **(Figures 10A, B).** In addition, the Rad-score in the allograft-CsA$_{cont}$ group showed a significantly higher value than the isograft group at week 6 ($P < 0.05$) **(Figures 10B)**. From week 3 to 6, there was an apparent decline in the allograft-CsA$_{delayed}$ group but not significant ($P = 0.108$) **(Figure 10C)**. The Rad-score for all recipient rats showed high positive correlations with A- and B-grade rejection and Fibrosis-(%), with coefficients of 0.857, 0.826, and 0.769, respectively ($P < 0.001$) **(Figures 10D, E, F)**.
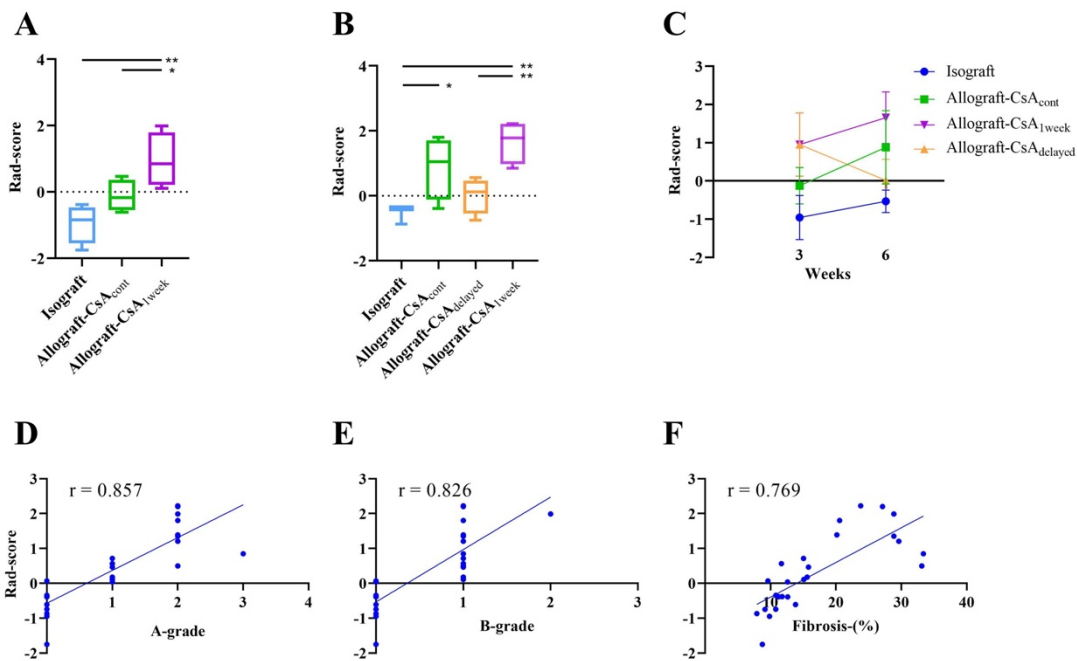
Figure 10: Correlations between Rad-score and histopathological AR criteria.
The Rad-score of each group at week 3 **(A)**, week 6 **(B)**, and changes in Rad-score from week 3 to week 6 **(C)**.
The Rad-score showed a positive correlation with A- **(D)** and B-grade rejection **(E)** and Fibrosis-(%) **(F)** with coefficients of 0.857, 0.826 and 0.769, respectively ($P < 0.001$).
* $P < 0.05$, ** $P < 0.01$, *** $P < 0.001$
r, Pearson's correlation coefficient; AR, allograft rejection; CsA, Cyclosporine; Rad-score, radiomics score; Fibrosis (%), percentage of parenchymal fibrosis.

3.3.5 Machine learning models

A total of 10, 10, 7, 12, 4, 7 radiomic features were selected for modeling in distance correlation, information gain, recursive feature elimination, Boruta algorithm, RF, and LASSO, respectively (**Table 3**). A total of 48 models were developed for predicting AR, including 42 ML models. The median AUC of the 42 ML models was 0.944 (0.878-0.978), which was superior to that of the 6 LR models (AUC = 0.794, 0.756-0.897) (**Figure 11**). The optimal ML model using the RF modeling algorithm with the RF feature selection method (RF-RF model) exhibited an AUC of 0.978 (95% confidence interval [CI], 0.936–1.000), which significantly outperformed the SUV $_{max}$ (AUC, 0.783; 95% CI, 0.602–0.964) (**Figure 12** and **Table 4**). Multidimensional scaling analysis showed rats with or without AR had a different distribution predicted by the RF-RF model (**Figure 13**). The original_GLDM_gray level non-uniformity (GLN) presented the most significant among the four selected features in the RF-RF model (**Figure 14**). In the DCA plot (**Figure 15**), the net benefit of the RF-RF was greater than the SUV$_{max}$ over all thresholds.

Table 3: Selected radiomic features in six algorithms.

Algorithms	Selected radiomic features
DC	Wavelet_LLL_GLCM_IMC 1
	Original_NGTDM_Busyness
	Wavelet_LHL_first-order_Median
	Original_GLDM_Gray Level Non-Uniformity
	Original_GLCM_IMC 1
	Original_GLCM_IMC 2

	Original_GLCM_Maximum Probability
	Original_first-order_Uniformity
	Original_GLRLM_Gray Level Non-Uniformity Normalized
	Original_GLRLM_Gray Level Non-Uniformity
IFGN	Wavelet_LLL_GLCM_Idm
	Wavelet_LLL_GLCM_Id
	Original_GLCM_Id
	Original_GLCM_Idm
	Wavelet_LLL_GLRLM_Run Length Non-Uniformity Normalized
	Wavelet_LLL_GLRLM_Short Run Emphasis
	Original_GLDM_Gray Level Non-Uniformity
	Wavelet_LLL_GLCM_IMC 1
	Wavelet_LHL_first-order_Median
	Original_GLCM_Sum Entropy
RFE	Original_GLCM_IMC 2
	Wavelet_LLL_GLCM_IMC 1
	Original_GLDM_Small Dependence High Gray Level Emphasis
	Wavelet_LHL_first-order_Median
	Original_NGTDM_Busyness
	Original_GLCM_IMC 1
	Wavelet_LLL_GLDM_High Gray Level Emphasis
Boruta	Original_GLDM_Gray Level Non-Uniformity

	Wavelet_LLH_GLSZM_Gray Level Non-Uniformity Normalized
	Wavelet_LHL_first-order_Median
	Wavelet_LHL_GLSZM_Large Area Emphasis
	Wavelet_LHH_GLRLM_Run Variance
	Wavelet_HHL_GLDM_Dependence Variance
	Wavelet_LLL_GLCM_IMC 1
	Wavelet_LLL_GLCM_MCC
	Wavelet_LLL_GLCM_Sum Average
	Wavelet_LLL_GLDM_High Gray Level Emphasis
	Wavelet_LLL_GLRLM_High Gray Level Run Emphasis
	Wavelet_LLL_GLRLM_Long Run High Gray Level Emphasis
RF	Original_GLDM_Gray Level Non-Uniformity
	Wavelet_LHL_first-order_Median
	Wavelet_LLL_GLCM_IMC 1
	Wavelet_LLL_GLCM_Joint Average
LASSO	Original_GLCM_IMC 2
	Original_GLCM_Maximum Probability
	Original_GLDM_Gray Level Non-Uniformity
	Original_GLRLM_RunVariance
	Original_NGTDM_Busyness
	Wavelet_LHL_first-order_Median
	Wavelet_LLL_GLCM_MCC

DC, distance correlation; IFGN, information gain; RFE, recursive feature elimination; RF, random forest; LASSO, least absolute shrinkage and selection operator; GLCM, gray level cooccurrence matrix; GLDM, gray level dependence matrix; NGTDM, neighboring gray tone difference matrix; GLRLM, gray level run length matrix; GLSZM, gray level size zone matrix; IMC, informational measure of correlation.
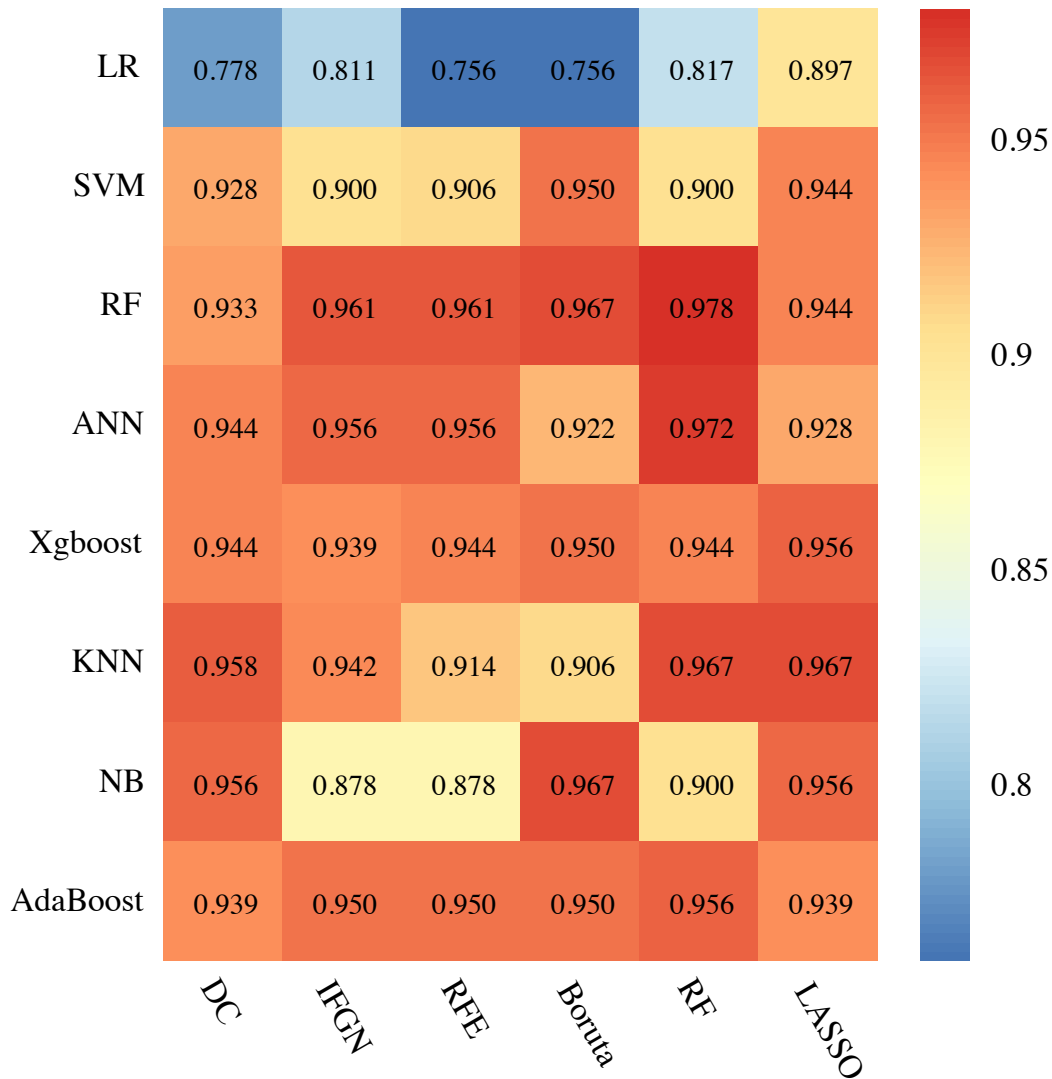
	DC	IFGN	RFE	Boruta	RF	LASSO
LR	0.778	0.811	0.756	0.756	0.817	0.897
SVM	0.928	0.900	0.906	0.950	0.900	0.944
RF	0.933	0.961	0.961	0.967	0.978	0.944
ANN	0.944	0.956	0.956	0.922	0.972	0.928
Xgboost	0.944	0.939	0.944	0.950	0.944	0.956
KNN	0.958	0.942	0.914	0.906	0.967	0.967
NB	0.956	0.878	0.878	0.967	0.900	0.956
AdaBoost	0.939	0.950	0.950	0.950	0.956	0.939

Figure 11: The performance of 48 prediction models.

A total of 48 models were developed for predicting AR, including 42 ML models.
The median AUC of ML models was 0.944 (0.878-0.978), which was superior to that of the LR model (AUC = 0.794, 0.756-0.897).
LR, logistic regression; SVM, support vector machine; RF, random forest; ANN, artificial neural network; Xgboost, extreme gradient boosting; KNN, k-nearest neighbors; NB, naive bayes; AdaBoost, adaptive boosting; DC, distance correlation; IFGN, information gain; RFE, recursive feature elimination; LASSO, least absolute shrinkage and selection operator; SUV, standardized uptake value.
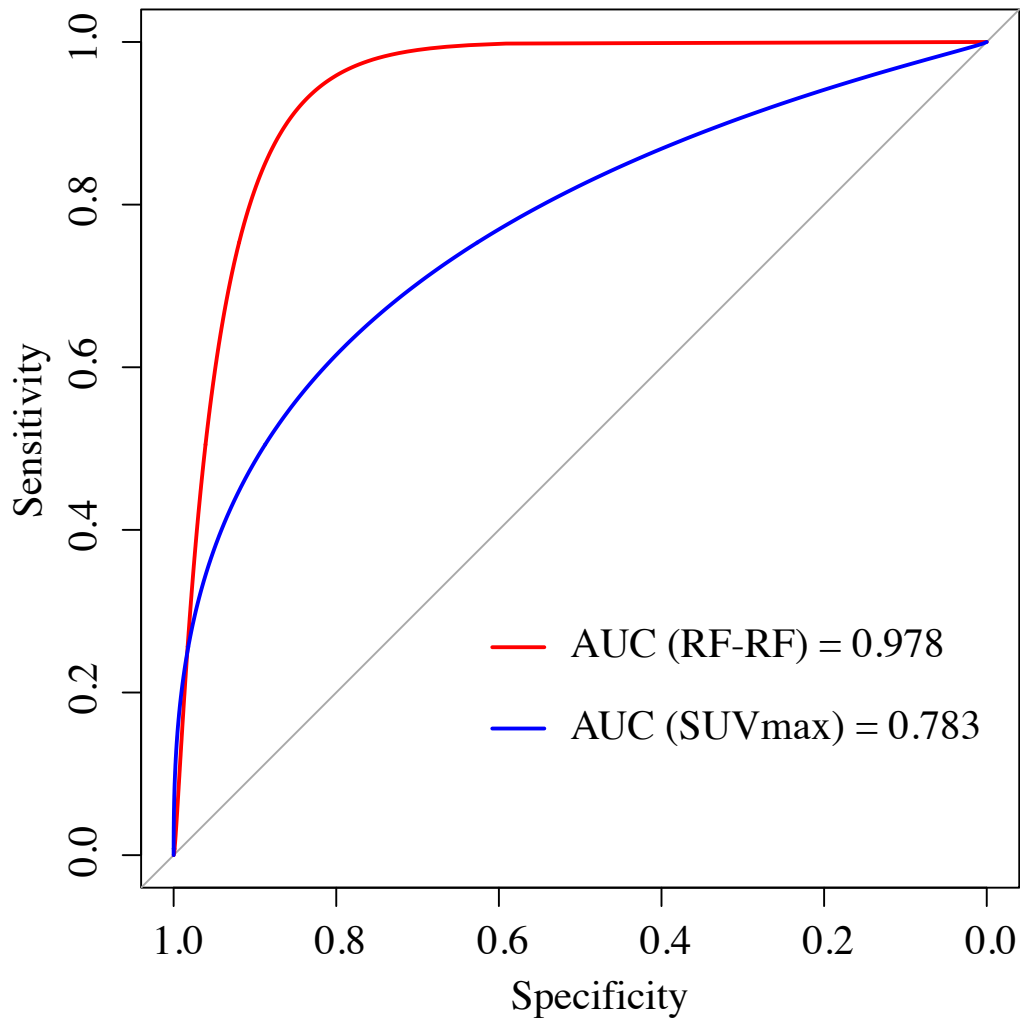
Figure 12: The receiver operator characteristic curve of optimal model and SUV$_{max}$.
AUC, area under the curve; RF, random forest; SUV$_{max}$, maximum standardized uptake value.

Table 4: The optimal model and SUV$_{max}$ for monitoring allograft rejection.

Model	AUC (95% CI)	Sensitivity	Specificity	PPV	NPV	Accuracy
RF-RF	0.978 (0.936-1.000)	100.0%	83.3%	88.2%	100.0%	92.6%
SUV$_{max}$	0.783 (0.602-0.964)	73.3%	83.3%	84.6%	71.4%	77.8%

AUC, area under the curve; CI, confidence interval; PPV, positive predictive value; NPV, negative predictive value; RF, random forest; SUV, standardized uptake value.
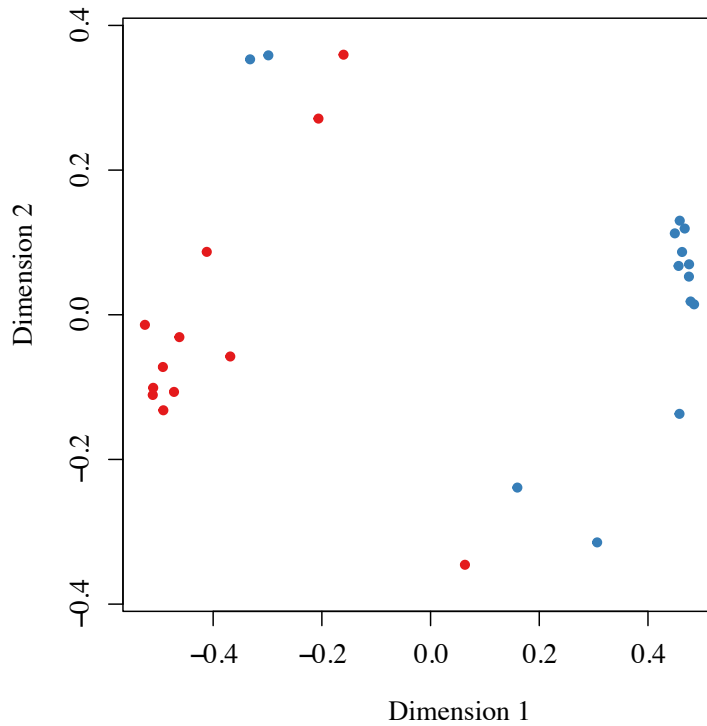
Figure 13: Multi-dimensional scaling of the proximity matrix.
Multidimensional scaling analysis showed rats with or without AR had a different distribution predicted by the optimal ML model (RF-RF model). The red and blue plots represented rats with AR and non-AR, respectively.
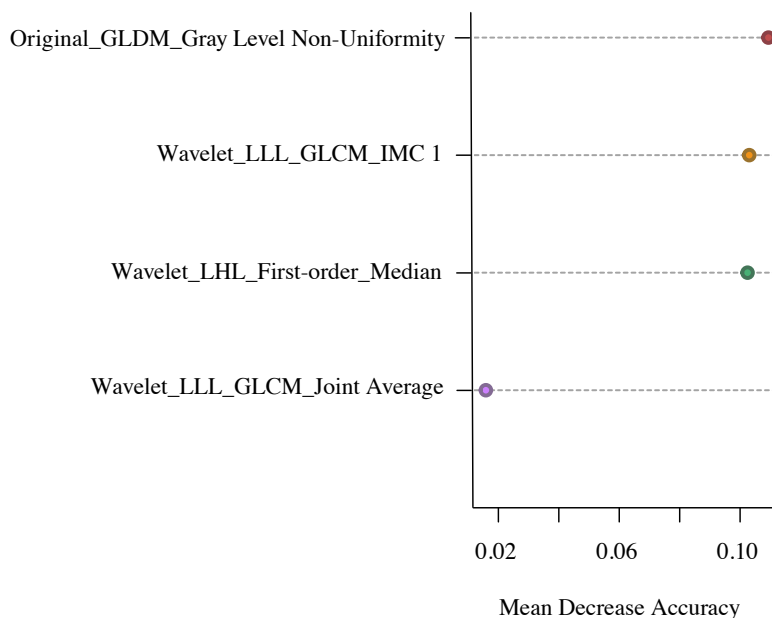RF, random forest.

Figure 14: Importance of the variables in the optimal random forest model.
The original_GLDM_GLN was the most significant feature among the four selected features in the random forest model.
GLDM, Gray Level Dependence Matrix; LLL, Low-Low-Low; GLCM, Gray Level Cooccurrence Matrix; IMC, Informational Measure of Correlation; LHL, low-high-low.
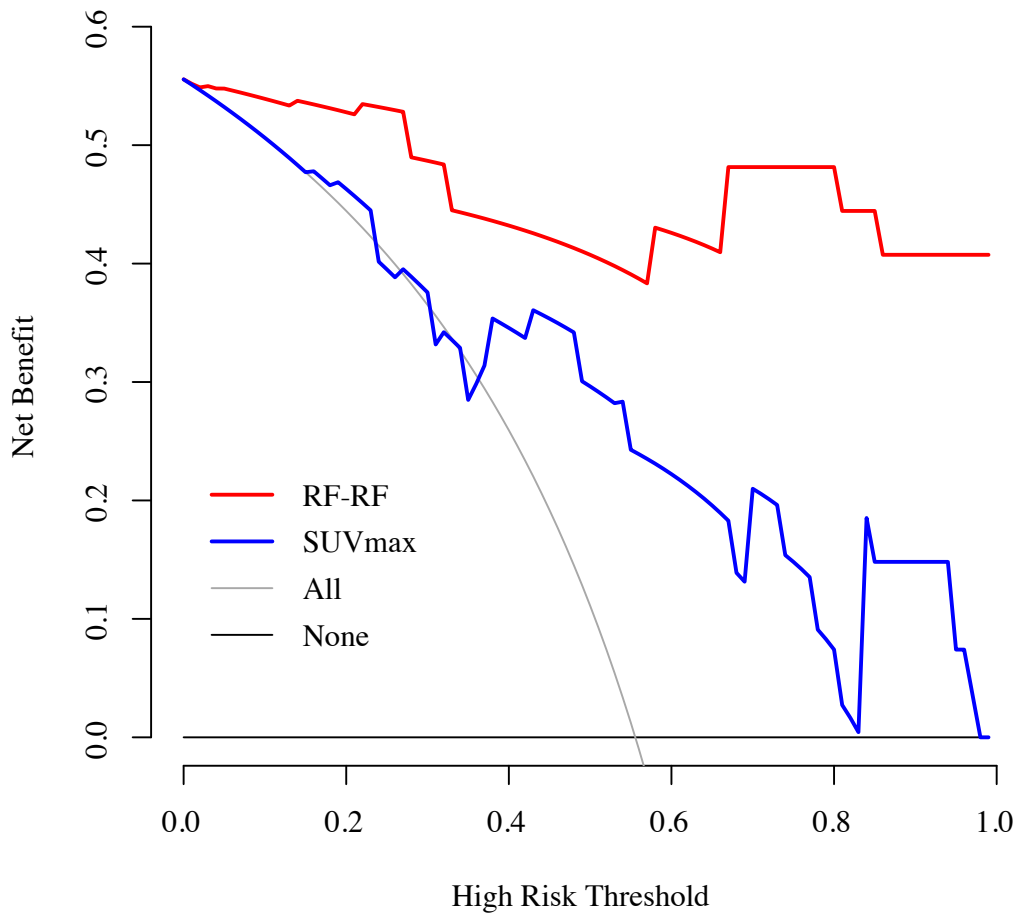
Figure 15: Decision curve analysis for optimal radiomics model and SUV$_{max}$.
The net benefit of the RF-RF was greater than the SUV$_{max}$ over all threshold.
RF, random forest; SUV$_{max}$, maximum standardized uptake value.

3.4 Discussion

The current study revealed two main findings. First, both the SUV$_{max}$ and Rad-score

showed significant positive correlations with the histopathological results. Second,

although the SUV$_{max}$ showed good discriminative power for AR, all the ML-based

radiomics models exhibited higher AUCs. These novel findings suggest that ML-based

18F-FDG PET radiomics has the potential to be a more effective noninvasive method for

monitoring AR following LTx.

PET is a noninvasive method of detecting rejection and assessing therapeutic efficacy

early after organ transplantations [33, 79]. Quantitative SUV parameters can be measured on 18F-FDG PET, and these can detect metabolic changes in tissues and evaluate the possibility of lung AR contributed to the amount of glucose consumption by T lymphocytes [44]. In the present study, the SUV_{max} was associated with pathological criteria indicating AR; however, the correlations were not satisfactory. Previous studies have shown that more useful information could be captured from PET radiomics, which offered value beyond conventional quantitative SUV parameters, providing additional information on AR [87, 88]. I extracted 837 radiomic features, and most of them were significantly correlated with the histopathological criteria for AR. Thus, the results strongly suggest that SUVs do not fully reflect the important information present in 18F-FDG PET images.

Most radiomics-related literature to date has been published in oncology; none has yet been published in the field of LTx. Only one recent study proposed that texture analysis applied to ultrashort echo-time magnetic resonance imaging might be useful for distinguishing AR in a mouse LTx model [49]. However, many features correlated with AR were not extracted from the images. Furthermore, the authors did not merge the texture features but only analyzed them separately [49]. Thus, their strategy could not reveal the inherent detective ability of radiomics for AR. I performed LASSO regression on the radiomics data and then merged the seven radiomic features to construct a Rad-score for AR. The Rad-score showed a strong correlation with the histopathological findings that covered various degrees of rejection. This indicates that the Rad-score has the potential to monitor AR in different stages. Additionally, the allograft-CsA$_{delayed}$ group

represented an AR treatment model, and this study demonstrated that PET radiomics analysis might have high performance for monitoring AR before an irreversible change develops.

Nevertheless, for the AR criteria, SUV_{max}, and Rad-score, the allograft CsA_{cont} group at week 6 showed higher values than in the isograft group. Rats might encounter pulmonary infection during the immunosuppressive maintenance treatment as clinical work [89, 90]. This further revealed that the infection and rejection might not be well differentiated by the conventional method based on 18F-FDG PET.

ML algorithms have made significant achievements in improving clinical detection and diagnosis. Barbosa et al. [51] found that an ML algorithm using quantitative computed tomography (CT) metrics could detect bronchiolitis obliterans syndrome with an accuracy of 85%. However, they only extracted conventional CT parameters instead of radiomic features and developed a single support vector machine model. Compared with CT, 18F-FDG PET can reveal more metabolic information from lung grafts. Very few studies have used ML models to improve the accuracy of lung AR detection, and these used rather limited ML models and information from biopsy and CT results [51, 52]. In this study, the DCA curve further revealed that the optimal ML model had the excellent ability to monitor AR and strengthened the monitoring value of 18F-FDG PET functional imaging for detecting AR in LTx. Notably, I found that the original_GLDM_GLN was the most significant radiomic feature for AR in the optimal model. It represents the similarity of intensity in the image where a lower original_GLDM_GLN indicates a more remarkable similarity in intensity [91]. This finding further demonstrated that radiomic

features contain more useful information for monitoring AR in addition to metabolic change. Compared with the SUV_{max}, which quantifies the total glucose metabolism in a lung graft with AR, radiomic features may potentially distinguish rejection from infection, but no evidence was found in this current study.

In clinical LTx, noninvasive methods for monitoring lung AR are currently being researched [51]. Radiomics is a widely used method involving the extraction of large numbers of features from radiological images using data-characterization algorithms. Its application will further enhance the value of radiological imaging in clinical practice, and radiomics based on 18F-FDG PET and ML algorithms may serve to decrease, but not eliminate, biopsy and potentially serve as a useful noninvasive method for postoperative lung AR.

3.5 Limitations

The following limitations of this study merit consideration. First, this pilot study may not sufficiently emulate the pathophysiological changes encountered in humans. Nonetheless, the current preclinical research forms a proof of concept. A move to human trials may be the only way to test the clinical relevance of the proposed methods. Second, I used the SUV_{max} to represent the ROI with the highest 18F-FDG uptake, but this did not provide information on differences between AR and respiratory infection. In human LTx, the differential diagnosis between AR and pneumonia may sometimes be difficult because 18F-FDG uptake is not disease-specific. However, infection was rare in this rodent model, even when non-sterile operations were performed, especially after a long post-LTx

duration. The allograft-CsA$_{delayed}$ group further confirmed AR at week three because immunosuppression therapy can reverse AR but not the infection. The histopathological results from hematoxylin–eosin staining, which can easily distinguish AR from respiratory infection, demonstrated a rare inflammatory process in this current preclinical study. Additionally, ML-based PET radiomics provided more information on the heterogeneity of lung grafts than the SUV$_{max}$ and may differentiate rejection from infection once the histopathologic features change in clinical LTx. Despite the strengths of 18F-FDG PET radiomics, the application of more specific radiotracers targeting different immune cells is expected [92, 93].

3.6 Conclusions

In conclusion, while both the SUV$_{max}$ and PET radiomics showed good correlations with AR, ML-based PET radiomics can further the value of functional imaging with 18F-FDG PET for monitoring AR in a rat LTx model. This current study supports further evaluation of the utility of this noninvasive method for detecting AR and monitoring the effectiveness of treatment for AR in clinical LTx.

References

[1] D.C. Chambers, W.S. Cherikh, M.O. Harhay, D. Hayes, E. Hsich, K.K. Khush, B. Meiser, L. Potena, J.W. Rossano, A.E. Toll, T.P. Singh, A. Sadavarte, A. Zuckermann, J. Stehlik, I.S.H.L. Transplantation, The International Thoracic Organ Transplant Registry of the International Society for Heart and Lung Transplantation: Thirty-sixth adult lung and heart-lung transplantation Report-2019; Focus theme: Donor and recipient size match, Journal of Heart and Lung Transplantation, 38 (2019) 1042-1055.

[2] K.C. Meyer, Recent advances in lung transplantation, F1000Res, 7 (2018).

[3] D.C. Chambers, R.D. Yusen, W.S. Cherikh, S.B. Goldfarb, A.Y. Kucheryavaya, K. Khusch, B.J. Levvey, L.H. Lund, B. Meiser, J.W. Rossano, J. Stehlik, I.S.H.L. Transplantation, The Registry of the International Society for Heart and Lung Transplantation: Thirty-fourth Adult Lung And Heart-Lung Transplantation Report 2017; Focus Theme: Allograft ischemic time, Journal of Heart and Lung Transplantation, 36 (2017) 1047-1059.

[4] G.M. Verleden, A.R. Glanville, E.D. Lease, A.J. Fisher, F. Calabrese, P.A. Corris, C.R. Ensor, J. Gottlieb, R.R. Hachem, V. Lama, T. Martinu, D.A.H. Neil, L.G. Singer, G. Snell, R. Vos, Chronic lung allograft dysfunction: Definition, diagnostic criteria, and approaches to treatment-A consensus report from the Pulmonary Council of the ISHLT, J Heart Lung Transplant, 38 (2019) 493-503.

[5] D.C. Chambers, W.S. Cherikh, S.B. Goldfarb, D. Hayes, A.Y. Kucheryavaya, A.E. Toll, K.K. Khush, B.J. Levvey, B. Meiser, J.W. Rossano, J. Stehlik, I.S.H.L. Transplantation, The International Thoracic Organ Transplant Registry of the

International Society for Heart and Lung Transplantation: Thirty-fifth adult lung and heart-lung transplant report-2018; Focus theme: Multiorgan Transplantation, Journal of Heart and Lung Transplantation, 37 (2018) 1169-1183.

[6] R.D. Yusen, L.B. Edwards, A.Y. Kucheryavaya, C. Benden, A.I. Dipchand, S.B. Goldfarb, B.J. Levvey, L.H. Lund, B. Meiser, J.W. Rossano, J. Stehlik, I.S.H.L. Transplantation, The Registry of the International Society for Heart and Lung Transplantation: Thirty-second Official Adult Lung and Heart-Lung Transplantation Report-2015; Focus Theme: Early Graft Failure, Journal of Heart and Lung Transplantation, 34 (2015) 1264-1277.

[7] G.M. Verleden, G. Raghu, K.C. Meyer, A.R. Glanville, P. Corris, A new classification system for chronic lung allograft dysfunction, Journal of Heart and Lung Transplantation, 33 (2014) 127-133.

[8] K.C. Meyer, G. Raghu, G.M. Verleden, P.A. Corris, P. Aurora, K.C. Wilson, J. Brozek, A.R. Glanville, I.A.E.B.T.F. Comm, An international ISHLT/ATS/ERS clinical practice guideline: diagnosis and management of bronchiolitis obliterans syndrome, Eur Respir J, 44 (2014) 1479-1503.

[9] M. Sato, T.K. Waddell, U. Wagnetz, H.C. Roberts, D.M. Hwang, A. Haroon, D. Wagnetz, C. Chaparro, L.G. Singer, M.A. Hutcheon, S. Keshavjee, Restrictive allograft syndrome (RAS): A novel form of chronic lung allograft dysfunction, Journal of Heart and Lung Transplantation, 30 (2011) 735-742.

[10] C.A. Pue, E.R. Pacht, Complications of Fiberoptic Bronchoscopy at a University Hospital, Chest, 107 (1995) 430-432.

[11] J. Rademacher, H. Suhling, M. Greer, A. Haverich, T. Welte, G. Warnecke, J. Gottlieb, Safety and efficacy of outpatient bronchoscopy in lung transplant recipients - a single centre analysis of 3,197 procedures, Transplant Res, 3 (2014) 11.

[12] A. Stephenson, J. Flint, J. English, S. Vedal, G. Fradet, D. Chittock, R.D. Levy, Interpretation of transbronchial lung biopsies from lung transplant recipients: inter- and intraobserver agreement, Can Respir J, 12 (2005) 75-77.

[13] C.M. Burke, J. Theodore, K.D. Dawkins, S.A. Yousem, N. Blank, M.E. Billingham, A. Van Kessel, S.W. Jamieson, P.E. Oyer, J.C. Baldwin, et al., Post-transplant obliterative bronchiolitis and other late lung sequelae in human heart-lung transplantation, Chest, 86 (1984) 824-829.

[14] M. Sato, Chronic lung allograft dysfunction after lung transplantation: the moving target, Gen Thorac Cardiovasc Surg, 61 (2013) 67-78.

[15] A. Van Muylem, C. Melot, M. Antoine, C. Knoop, M. Estenne, Role of pulmonary function in the detection of allograft dysfunction after heart-lung transplantation, Thorax, 52 (1997) 643-647.

[16] M. Estenne, J.R. Maurer, A. Boehler, J.J. Egan, A. Frost, M. Hertz, G.B. Mallory, G.I. Snell, S. Yousem, Bronchiolitis obliterans syndrome 2001: an update of the diagnostic criteria, J Heart Lung Transplant, 21 (2002) 297-310.

[17] D.P. Mason, J. Rajeswaran, S.C. Murthy, A.M. McNeill, M.M. Budev, A.C. Mehta, G.B. Pettersson, E.H. Blackstone, Spirometry after transplantation: how much better are two lungs than one?, Ann Thorac Surg, 85 (2008) 1193-1201, 1201 e1191-1192.

[18] J.A. Shepard, Imaging of lung transplantation, Clin Chest Med, 20 (1999) 827-844,

ix.

[19] S.J. Herman, G.L. Weisbrod, L. Weisbrod, G.A. Patterson, J.R. Maurer, Chest Radiographic Findings after Bilateral Lung Transplantation, Am J Roentgenol, 153 (1989) 1181-1185.

[20] J. Collins, Imaging of the chest after lung transplantation, J Thorac Imag, 17 (2002) 102-112.

[21] A. Di Piazza, G. Mamone, S. Caruso, G. Marrone, F. Tuzzolino, P. Vitulo, A. Bertani, R. Miraglia, Acute rejection after lung transplantation: association between histopathological and CT findings, Radiol Med, 124 (2019) 1000-1005.

[22] M.B. Gotway, S.K. Dawn, D. Sellami, J.A. Golden, G.P. Reddy, F.M. Keith, W.R. Webb, Acute rejection following lung transplantation: limitations in accuracy of thin-section CT for diagnosis, Radiology, 221 (2001) 207-212.

[23] P.A. de Jong, J.D. Dodd, H.O. Coxson, C. Storness-Bliss, P.D. Pare, J.E. Mayo, R.D. Levy, Bronchiolitis obliterans following lung transplantation: early detection using computed tomographic scanning, Thorax, 61 (2006) 799-804.

[24] A. Voskrebenzev, M. Gutberlet, T.F. Kaireit, F. Wacker, J. Vogel-Claussen, Low-pass imaging of dynamic acquisitions (LIDA) with a group-oriented registration (GOREG) for proton MR imaging of lung ventilation, Magn Reson Med, 78 (2017) 1496-1505.

[25] T.M. Alsady, A. Voskrebenzev, M. Greer, L. Becker, T.F. Kaireit, T. Welte, F. Wacker, J. Gottlieb, J. Vogel-Claussen, MRI-derived regional flow-volume loop parameters detect early-stage chronic lung allograft dysfunction, Journal of Magnetic Resonance Imaging, 50 (2019) 1873-1882.

[26] S. Siddiqui, A. Habertheuer, Y. Xin, M. Pourfathi, J.Q. Tao, H. Hamedani, S. Kadlecek, I. Duncan, P. Vallabhajosyula, A. Naji, S. Chatterjee, R. Rizi, Detection of lung transplant rejection in a rat model using hyperpolarized [1-C-13] pyruvate-based metabolic imaging, Nmr Biomed, 32 (2019).

[27] J.R. Davidsen, C.B. Laursen, E. Bendstrup, H.H.L. Schultz, Lung Ultrasound - A Novel Diagnostic Tool To Phenotype Chronic Lung Allograft Dysfunction?, Ultrasound Int Open, 3 (2017) E117-E119.

[28] J.R. Davidsen, H.H.L. Schultz, D.P. Henriksen, M. Iversen, A. Kalhauge, J. Carlsen, M. Perch, O. Graumann, C.B. Laursen, Lung Ultrasound in the Assessment of Pulmonary Complications After Lung Transplantation, Ultraschall Med, (2018).

[29] P. Diana, D. Zampiere, E. Furlani, E. Pivetta, F. Calabrese, F. Pezzuto, G. Marulli, F. Rea, C. Ori, P. Persona, Lung ultrasound as a monitoring tool in lung transplantation in rodents: a feasibility study, Journal of Thoracic Disease, 10 (2018) 4274-4282.

[30] K.S. Ayyat, T. Okamoto, H. Niikawa, Y. Itoda, S. Dugar, S.Q. Latifi, D.J. Lebovitz, A. Moghekar, K.R. McCurry, DireCt Lung Ultrasound Evaluation (CLUE): A novel technique for monitoring extravascular lung water in donor lungs, Journal of Heart and Lung Transplantation, 38 (2019) 757-766.

[31] T. Narula, A. Banga, D. Sahoo, S. Krishnan, X. Han, X. Wang, M.M. Budev, A.C. Mehta, A. Moghekar, Lung Ultrasound to Detect Allograft Dysfunction in Lung Transplant Recipients, Am J Resp Crit Care, 199 (2019).

[32] A.B. Tsuji, M. Morita, X.K. Li, C. Sogawa, H. Sudo, A. Sugyo, M. Fujino, A. Sugioka, M. Koizumi, T. Saga, F-18-FDG PET for Semiquantitative Evaluation of Acute

Allograft Rejection and Immunosuppressive Therapy Efficacy in Rat Models of Liver

Transplantation, Journal of Nuclear Medicine, 50 (2009) 827-830.

[33] K.P. Daly, J.L. Dearling, T. Seto, P. Dunning, F. Fahey, A.B. Packard, D.M. Briscoe,

Use of [18F]FDG Positron Emission Tomography to Monitor the Development of

Cardiac Allograft Rejection, Transplantation, 99 (2015) e132-139.

[34] P. Lovinfosse, L. Weekers, C. Bonvoisin, C. Bovy, S. Grosch, J.M. Krzesinski, R.

Hustinx, F. Jouret, Fluorodeoxyglucose F(18) Positron Emission Tomography Coupled

With Computed Tomography in Suspected Acute Renal Allograft Rejection, Am J

Transplant, 16 (2016) 310-316.

[35] S.E. Verleden, O. Gheysens, K.E. Goffin, B.M. Vanaudenaerde, E.K. Verbeken, B.

Weynand, D.E. Van Raemdonck, G.M. Verleden, R. Vos, Role of 18F-FDG PET/CT in

Restrictive Allograft Syndrome After Lung Transplantation, Transplantation, 103 (2019)

823-831.

[36] S.J. Hoff, J.R. Stewart, W.H. Frist, J.B. Atkinson, M.W. Kronenberg, J. Votaw, R.M.

Kessler, M.P. Sandler, Noninvasive Detection of Acute Rejection in a New Experimental-

Model of Heart-Transplantation, Annals of Thoracic Surgery, 56 (1993) 1074-1077.

[37] A.M. Watson, N. Bhutiani, P. Philips, E.G. Davis, M. Eng, R.M. Cannon, C.M. Jones,

The role of FDG-PET in detecting rejection after liver transplantation, Surgery, 164 (2018)

257-261.

[38] F. Jamar, J. Buscombe, A. Chiti, P.E. Christian, D. Delbeke, K.J. Donohoe, O. Israel,

J. Martin-Comin, A. Signore, EANM/SNMMI Guideline for F-18-FDG Use in

Inflammation and Infection, Journal of Nuclear Medicine, 54 (2013) 647-658.

[39] E.Y.P. Lee, C.S. Wong, S.L. Fung, P.K. Yan, J.C.M. Ho, SUV as an adjunct in evaluating disease activity in idiopathic pulmonary fibrosis - a pilot study, Nucl Med Commun, 35 (2014) 631-637.

[40] A.M. Groves, T. Win, N.J. Screaton, M. Berovic, R. Endozo, H. Booth, I. Kayani, L.J. Menezes, J.C. Dickson, P.J. Ell, Idiopathic Pulmonary Fibrosis and Diffuse Parenchymal Lung Disease: Implications from Initial Experience with F-18-FDG PET/CT, Journal of Nuclear Medicine, 50 (2009) 538-545.

[41] W. Van Rompaey, O. Gheysens, C.M. Deroose, S.E. Verleden, B.M. Vanaudenaerde, L.J. Ceulemans, D.E. Van Raemdonck, A.P. Neyrinck, G.M. Verleden, R. Vos, Diagnostic Yield of 18F-FDG PET After Lung Transplantation: A Single-center, Retrospective Cohort Study, Transplantation, 105 (2021) 1603-1609.

[42] T. Ertay, M.S. Eren, M. Karaman, G. Oktay, H. Durak, F-18-FDG-PET/CT in Initiation and Progression of Inflammation and Infection, Mol Imaging Radionuc, 26 (2017) 47-52.

[43] S. Capitanio, A.J. Nordin, A.R. Noraini, C. Rossetti, PET/CT in nononcological lung diseases: current applications and future perspectives, Eur Respir Rev, 25 (2016) 247-258.

[44] D.L. Chen, X. Wang, S. Yamamoto, D. Carpenter, J.T. Engle, W. Li, X. Lin, D. Kreisel, A.S. Krupnick, H.J. Huang, A.E. Gelman, Increased T cell glucose uptake reflects acute rejection in lung grafts, Am J Transplant, 13 (2013) 2540-2549.

[45] H.A. Jones, T. Donovan, M.J. Goddard, K. McNeil, C. Atkinson, J.C. Clark, J.F. White, E.R. Chilvers, Use of (18)FDG-PET to discriminate between infection and rejection in lung transplant recipients, Transplantation, 77 (2004) 1462-1464.

[46] R. Vos, S.E. Verleden, D. Ruttens, E. Vandermeulen, J. Yserbyt, L.J. Dupont, D.E. Van Raemdonck, N. De Raedt, O. Gheysens, P.A. De Jong, G.M. Verleden, B.M. Vanaudenaerde, Pirfenidone: A Potential New Therapy for Restrictive Allograft Syndrome?, American Journal of Transplantation, 13 (2013) 3035-3040.

[47] G.J.R. Cook, M. Siddique, B.P. Taylor, C. Yip, S. Chicklore, V. Goh, Radiomics in PET: principles and applications, Clinical and Translational Imaging, 2 (2014) 269-276.

[48] M.D. Kuo, N. Jamshidi, Behind the numbers: Decoding molecular phenotypes with radiogenomics--guiding principles and technical considerations, Radiology, 270 (2014) 320-325.

[49] A. Euler, C. Bluthgen, M.C. Wurnig, W. Jungraithmayr, A. Boss, Can texture analysis in ultrashort echo-time MRI distinguish primary graft dysfunction from acute rejection in lung transplants? A multidimensional assessment in a mouse model, J Magn Reson Imaging, 51 (2020) 108-116.

[50] G. Choy, O. Khalilzadeh, M. Michalski, S. Do, A.E. Samir, O.S. Pianykh, J.R. Geis, P.V. Pandharipande, J.A. Brink, K.J. Dreyer, Current Applications and Future Impact of Machine Learning in Radiology, Radiology, 288 (2018) 318-328.

[51] E.J.M. Barbosa, Jr., M. Lanclus, W. Vos, C. Van Holsbeke, W. De Backer, J. De Backer, J. Lee, Machine Learning Algorithms Utilizing Quantitative CT Features May Predict Eventual Onset of Bronchiolitis Obliterans Syndrome After Lung Transplantation, Acad Radiol, 25 (2018) 1201-1212.

[52] K.M. Halloran, M.D. Parkes, J. Chang, I.L. Timofte, G.I. Snell, G.P. Westall, R. Hachem, D. Kreisel, E. Trulock, A. Roux, S. Juvet, S. Keshavjee, P. Jaksch, W. Klepetko,

P.F. Halloran, Molecular assessment of rejection and injury in lung transplant biopsies, J Heart Lung Transplant, 38 (2019) 504-513.

[53] T. Mizuta, A. Kawaguchi, K. Nakahara, Y. Kawashima, Simplified Rat Lung Transplantation Using a Cuff Technique, J Thorac Cardiov Sur, 97 (1989) 578-581.

[54] M. Okazaki, A.S. Krupnick, C.G. Kornfeld, J.M. Lai, J.H. Ritter, S.B. Richardson, H.J. Huang, N.A. Das, G.A. Patterson, A.E. Gelman, D. Kreisel, A mouse model of orthotopic vascularized aerated lung transplantation, American Journal of Transplantation, 7 (2007) 1672-1679.

[55] W. Zhai, J. Ge, I. Inci, S. Hillinger, C. Markus, S. Korom, W. Weder, Simplified rat lung transplantation by using a modified cuff technique, J Invest Surg, 21 (2008) 33-37.

[56] T. Goto, M. Kohno, M. Anraku, T. Ohtsuka, Y. Izumi, H. Nomori, Simplified Rat Lung Transplantation Using a New Cuff Technique, Annals of Thoracic Surgery, 93 (2012) 2078-2080.

[57] H.Z. Guo, J. Nie, K. Fan, Z.K. Zheng, X.W. Qiao, J.S. Li, J.J. Wang, K. Jiang, Improvements of surgical techniques in a rat model of an orthotopic single lung transplant, Eur J Med Res, 18 (2013).

[58] D. Zampieri, N. Azzollini, S. Vuljan, F. Pezzuto, S. Fiori, M. Mister, M. Todeschini, P.Y. Rodriguez Ordonez, G. Marulli, F. Rea, F. Calabrese, F. Casiraghi, Vein Suturing Results in Worse Lung Graft Outcomes Compared to the Cuff Method, Eur Surg Res, 60 (2019) 106-116.

[59] B. Kubisa, R.A. Schmid, T. Grodzki, Model of single left rat lung transplantation. Relation between surgical experience and outcomes, Rocz Akad Med Bialymst, 48 (2003)

70-73.

[60] E. Miyamoto, H. Motoyama, M. Sato, A. Aoyama, T. Menju, K. Shikuma, T. Sowa, A. Yoshizawa, M. Saito, A. Takahagi, S. Tanaka, M. Takahashi, K. Ohata, T. Kondo, K. Hijiya, T.F. Chen-Yoshikawa, H. Date, Association of Local Intrapulmonary Production of Antibodies Specific to Donor Major Histocompatibility Complex Class I With the Progression of Chronic Rejection of Lung Allografts, Transplantation, 101 (2017) e156-e165.

[61] A. Takahagi, T. Shindo, T.F. Chen-Yoshikawa, A. Yoshizawa, F. Gochi, E. Miyamoto, M. Saito, S. Tanaka, H. Motoyama, A. Aoyama, A. Takaori-Kondo, H. Date, Trametinib Attenuates Delayed Rejection and Preserves Thymic Function in Rat Lung Transplantation, Am J Resp Cell Mol, 61 (2019) 355-366.

[62] R. Sugimoto, A. Nakao, I. Nagahiro, J. Kohmoto, S. Sugimoto, M. Okazaki, M. Yamane, H. Inokawa, T. Oto, K. Tahara, J. Zhan, Y. Sano, K.R. McCurry, Experimental orthotopic lung transplantation model in rats with cold storage, Surg Today, 39 (2009) 641-645.

[63] W.J. Li, S. Sugimoto, J.M. Lai, G.A. Patterson, A.E. Gelman, A.S. Krupnick, D. Kreisel, Orthotopic vascularized right lung transplantation in the mouse, J Thorac Cardiov Sur, 139 (2010) 1637-1643.

[64] T.K. Rajab, Anastomotic techniques for rat lung transplantation, World J Transplant, 8 (2018) 38-43.

[65] A. Habertheuer, A. Kocher, G. Laufer, P. Petzelbauer, M. Andreas, S. Aharinejad, M. Ehrlich, D. Wiedemann, Innovative, simplified orthotopic lung transplantation in rats,

Journal of Surgical Research, 185 (2013) 419-425.

[66] K.W. Marck, C.R. Wildevuur, Lung transplantation in the rat: I. Technique and survival, Ann Thorac Surg, 34 (1982) 74-80.

[67] W. Jungraithmayr, W. Weder, The Technique of Orthotopic Mouse Lung Transplantation as a Movie - Improved Learning by Visualization, American Journal of Transplantation, 12 (2012) 1624-1626.

[68] H. Suzuki, L. Fan, D.S. Wilkes, Development of Obliterative Bronchiolitis in a Murine Model of Orthotopic Lung Transplantation, Jove-J Vis Exp, (2012).

[69] W.M. Jungraithmayr, S. Korom, S. Hillinger, W. Weder, A mouse model of orthotopic, single-lung transplantation, J Thorac Cardiov Sur, 137 (2009) 486-491.

[70] M.S. Bhabra, D.N. Hopkinson, T.E. Shaw, T.L. Hooper, Critical importance of the first 10 minutes of lung graft reperfusion after hypothermic storage, Annals of Thoracic Surgery, 61 (1996) 1631-1635.

[71] M.S. Bhabra, D.N. Hopkinson, T.E. Shaw, N. Onwu, T.L. Hooper, Controlled reperfusion protects lung grafts during a transient early increase in permeability, Annals of Thoracic Surgery, 65 (1998) 187-192.

[72] A.F. Pierre, K.N. DeCampos, M.Y. Liu, V. Edwards, E. Cutz, A.S. Slutsky, S.H. Keshavjee, Rapid reperfusion causes stress failure in ischemic rat lungs, J Thorac Cardiov Sur, 116 (1998) 932-942.

[73] M. Hartert, O. Senbaklavacin, B. Gohrbandt, B.M. Fischer, R. Buhl, C.F. Vahld, Lung transplantation: a treatment option in end-stage lung disease, Dtsch Arztebl Int, 111 (2014) 107-116.

[74] R.R. Hachem, Acute Rejection and Antibody-Mediated Rejection in Lung Transplantation, Clin Chest Med, 38 (2017) 667-675.

[75] A. Van Herck, S.E. Verleden, B.M. Vanaudenaerde, G.M. Verleden, R. Vos, Prevention of chronic rejection after lung transplantation, J Thorac Dis, 9 (2017) 5472-5488.

[76] A.D. Parulekar, C.C. Kao, Detection, classification, and management of rejection after lung transplantation, J Thorac Dis, 11 (2019) S1732-S1739.

[77] M. Greer, C. Werlein, D. Jonigk, Surveillance for acute cellular rejection after lung transplantation, Ann Transl Med, 8 (2020) 410.

[78] D. Tian, H. Huang, H.Y. Wen, Noninvasive methods for detection of chronic lung allograft dysfunction in lung transplantation, Transplant Rev (Orlando), 34 (2020) 100547.

[79] A. Grabner, D. Kentrup, U. Schnockel, G. Gabriels, R. Schroter, H. Pavenstadt, O. Schober, E. Schlatter, M. Schafers, S. Reuter, Non-invasive imaging of acute allograft rejection after rat renal transplantation using 18F-FDG PET, J Vis Exp, (2013) e4240.

[80] D. Tian, H. Shiiya, M. Sato, J. Nakajima, Rat lung transplantation model: modifications of the cuff technique., Ann Transl Med, 8 (2020) 1-9.

[81] S. Stewart, M.C. Fishbein, G.I. Snell, G.J. Berry, A. Boehler, M.M. Burke, A. Glanville, F.K. Gould, C. Magro, C.C. Marboe, K.D. McNeil, E.F. Reed, N.L. Reinsmoen, J.P. Scott, S.M. Studer, H.D. Tazelaar, J.L. Wallwork, G. Westall, M.R. Zamora, A. Zeevi, S.A. Yousem, Revision of the 1996 working formulation for the standardization of nomenclature in the diagnosis of lung rejection, J Heart Lung Transplant, 26 (2007) 1229-

1242.

[82] J.J.M. van Griethuysen, A. Fedorov, C. Parmar, A. Hosny, N. Aucoin, V. Narayan, R.G.H. Beets-Tan, J.C. Fillion-Robin, S. Pieper, H. Aerts, Computational Radiomics System to Decode the Radiographic Phenotype, Cancer Res, 77 (2017) e104-e107.

[83] S. van der Walt, J.L. Schonberger, J. Nunez-Iglesias, F. Boulogne, J.D. Warner, N. Yager, E. Gouillart, T. Yu, c. scikit-image, scikit-image: image processing in Python, PeerJ, 2 (2014) e453.

[84] Z. Qian, Y. Li, Y. Wang, L. Li, R. Li, K. Wang, S. Li, K. Tang, C. Zhang, X. Fan, B. Chen, W. Li, Differentiation of glioblastoma from solitary brain metastases using radiomic machine-learning classifiers, Cancer Lett, 451 (2019) 128-135.

[85] G. Berra, S. Farkona, Z. Mohammed-Ali, M. Kotlyar, L. Levy, S. Clotet-Freixas, P. Ly, B. Renaud-Picard, G. Zehong, T. Daigneault, A. Duong, I. Batruch, I. Jurisica, A. Konvalinka, T. Martinu, Association between renin-angiotensin system and chronic lung allograft dysfunction, Eur Respir J, (2021).

[86] P.M. van Oort, P. Brinkman, G. Slingers, G. Koppen, A. Maas, J.J. Roelofs, R. Schnabel, D.C. Bergmans, M. Raes, R. Goodacre, S.J. Fowler, M.J. Schultz, L.D. Bos, Exhaled breath metabolomics reveals a pathogen-specific response in a rat pneumonia model for two human pathogenic bacteria: a proof-of-concept study, Am J Physiol Lung Cell Mol Physiol, 316 (2019) L751-L756.

[87] J. Zhang, X. Zhao, Y. Zhao, J. Zhang, Z. Zhang, J. Wang, Y. Wang, M. Dai, J. Han, Value of pre-therapy (18)F-FDG PET/CT radiomics in predicting EGFR mutation status in patients with non-small cell lung cancer, Eur J Nucl Med Mol Imaging, 47 (2020) 1137-

1146.

[88] M. Hatt, F. Tixier, D. Visvikis, C. Cheze Le Rest, Radiomics in PET/CT: More Than Meets the Eye?, J Nucl Med, 58 (2017) 365-366.

[89] S. Atanasova, M. Hirschburger, D. Jonigk, M. Obert, K. Petri, A. Evers, A. Hecker, J. Schmitz, A. Kaufmann, J. Wilhelm, T. Chakraborty, G. Warnecke, J. Gottlieb, W. Padberg, V. Grau, A relevant experimental model for human bronchiolitis obliterans syndrome, J Heart Lung Transplant, 32 (2013) 1131-1139.

[90] A.B. Watts, J.I. Peters, R.L. Talbert, K.P. O'Donnell, J.J. Coalson, R.O. Williams, 3rd, Preclinical evaluation of tacrolimus colloidal dispersion for inhalation, Eur J Pharm Biopharm, 77 (2011) 207-215.

[91] Y. Li, M. Yu, G. Wang, L. Yang, C. Ma, M. Wang, M. Yue, M. Cong, J. Ren, G. Shi, Contrast-Enhanced CT-Based Radiomics Analysis in Predicting Lymphovascular Invasion in Esophageal Squamous Cell Carcinoma, Front Oncol, 11 (2021) 644165.

[92] M.Y. Stevens, H.C. Cropper, K.L. Lucot, A.M. Chaney, K.J. Lechtenberg, I.M. Jackson, M.S. Buckwalter, M.L. James, Development of a CD19 PET tracer for detecting B cells in a mouse model of multiple sclerosis, J Neuroinflammation, 17 (2020) 275.

[93] J. Schniering, M. Benesova, M. Brunner, S. Haller, S. Cohrs, T. Frauenfelder, B. Vrugt, C. Feghali-Bostwick, R. Schibli, O. Distler, C. Muller, B. Maurer, (18)F-AzaFol for Detection of Folate Receptor-beta Positive Macrophages in Experimental Interstitial Lung Disease-A Proof-of-Concept Study, Front Immunol, 10 (2019) 2724.

Acknowledgements

Throughout my research on the Doctoral Program of Medicine, I have received a great deal of support and assistance.

Appendices

List of publications

1. Published

[1] Haruhiko Shiiya, **Dong Tian**, Masaaki Sato, Takahiro Karasaki, Kentaro Kitano, Kazuhiro Nagayama, Masaki Anraku, Kichizo Kaga, Yoshiro Matsui, Jun Nakajima. Differences Between Patients With Idiopathic Pleuroparenchymal Fibroelastosis and Those With Other Types of Idiopathic Interstitial Pneumonia in Candidates for Lung Transplants. Transplant Proc. 2019;51(6):2014-2021.

[2] **Dong Tian**, Haruhiko Shiiya, Masaaki Sato, Chang-Bo Sun, Masaki Anraku, Jun Nakajima. Tumor location may affect the clinicopathological features and prognosis of thymomas. Thoracic Cancer. 2019, 10(11):2096-2105.

[3] **Dong Tian**, Yu Wang, Haruhiko Shiiya, Chang-Bo Sun, Yukari Uemura, Masaaki Sato, Jun Nakajima. Clinical Outcomes in Lung Transplantation of Marginal Donor after Ex vivo Lung Perfusion: A Systematic Review and Meta-analysis. The Journal of Thoracic and Cardiovascular Surgery, 2020, 159(2): 720-730.

[4] **Dong Tian**, Haruhiko Shiiya, Masaaki Sato, Jun Nakajima. Rat lung transplantation model: modifications of the cuff technique. Ann Transl Med, 2020, 8(6). doi: 10.21037/atm.2020.02.46.

[5] Masaaki Sato, **Dong Tian (co- Corresponding author)**. Strategies to achieve long-term success of lung transplantation. Ann Transl Med, 2020;8(6):406. doi: 10.21037/atm.2020.02.160.

[6] **Dong Tian**, Heng Huang, Hong-Ying Wen. Noninvasive Methods for Detection of

Chronic Lung Allograft Dysfunction in Lung Transplantation. Transplant Rev (Orlando). 2020,34(4): 100547. https://doi.org/10.1016/j.trre.2020.100547.

[7] **Dong Tian**, Haruhiko Shiiya, Masaaki Sato, Jun Nakajima. Tumor Maximum Area May Determine the Survival Outcomes of Patients with Thymic Epithelial Tumors. Ann Surg Oncol. 2021 Apr;28(4):2078-2085.

[8] **Dong Tian**, Haoji Yan, Jun Nakajima. ASO Author Reflections: Tumor Maximum Area is Better for Representing Tumor Size in Thymic Epithelial Tumors. Ann Surg Oncol. 2021 Apr;28(4):2086-2087.

[9] **Dong Tian**, Jun Nakajima. Reply to "Euclidean Geometry Versus Metabolic Biochemistry in the Prognostic Evaluation of the Thymic Epithelial Tumours". Ann Surg Oncol. 2020, 28(7):4060-4061.

[10] **Dong Tian**, Haruhiko Shiiya, Miwako Takahashi, Yasuhiro Terasaki, Hirokazu Urushiyama, Aya Shinozaki-Ushiku, Masaaki Sato, Jun Nakajima. Application of Radiomics Based on 18F-fluorodeoxyglucose Positron Emission Tomography for Predicting of Allograft Rejection in a Rat Lung Transplantation Model. J Heart Lung Transplant. 2021, 40(4): S150-S151.

[11] Masaaki Sato, Shun-Mao Yang, **Dong Tian,** Nakajima Jun, Jang-Ming Lee. Managing screening-detected subsolid nodules—the Asian perspective. Transl Lung Cancer Res. 2021, 10(5):2323-2334.

2. In preparation (Submitted)

[1] **Dong Tian**, Haruhiko Shiiya, Miwako Takahashi, Yasuhiro Terasaki, Hirokazu Urushiyama, Aya Shinozaki-Ushiku, Hao-Ji Yan, Masaaki Sato, Jun Nakajima. Noninvasive monitoring of allograft rejection in a rat lung transplant model: Application of machine learning-based 18F- fluorodeoxyglucose positron emission tomography radiomics. (under review).

[2] **Dong Tian**, Haruhiko Shiiya, Masaaki Sato, Aya Shinozaki-Ushiku, Hao-Ji Yan, Jun Nakajima. Pathologic Tumor Long-to-short Axis Ratio as A Prognostic Factor in Patients with Thymic Epithelial Tumors. (under review).

[3] **Dong Tian**, Hao-Ji Yan, Haruhiko Shiiya, Masaaki Sato, Aya Shinozaki-Ushiku, Jun Nakajima. Machine learning-based radiomic computed tomography phenotyping of thymic epithelial tumours: Predicting pathological and survival outcomes. (under review).

3. Special Issue

[1] Masaaki Sato, **Dong Tian (co-Guest Editor)**. Strategies to achieve long-term success of lung transplantation. Ann Transl Med, 2020;8(6). Totally one original paper and 11 review papers were organized in this issue.

List of conference presentations

[1] May 15, 2022, 102nd AATS Annual Meeting, Oral presentation, Boston, USA.

[2] Apr. 30, 2022, 42nd ISHLT Annual Meeting, Invited presentation in a Symposium Session, Boston, USA.

[3] Feb. 11, 2022, The Annual Meeting of 41st Japanese Association for Research on the Thymus. Oral presentation, Chiba, Japan.

[4] Nov. 2, 2021, The 74th Annual Meeting of the Japanese Association for Thoracic Surgery, Oral presentation, Tokyo, Japan.

[5] Apr. 24, 2021, 41st ISHLT Annual Meeting, Oral presentation, Virtual.

[6] Oct. 2, 2020, 1th European Society of Thoracic Surgeons (ESTS) Virtual Meeting. Oral presentation.

[7] Feb. 15, 2020, The Annual Meeting of 39th Japanese Association for Research on the Thymus. Oral presentation, Sapporo, Japan.

[8] Nov. 3, 2019, Pengcheng Seminar on Organ Transplantation, Oral presentation, Shenzhen, China.

[9] Nov. 2, 2019, Wuxi International Lung Transplantation Conference, Oral presentation, Wuxi, China.

[10] May 17, 2019, The 36th Annual Meeting of Japanese Association for Chest Surgery (JACS). Oral presentation. Osaka, Japan.